Asymmetries in Surface Temperature Distribution of Neutron Stars

A Thesis

submitted to
Indian Institute of Science Education and Research Pune
in partial fulfillment of the requirements for the
BS-MS Dual Degree Programme

by

Varun Shah

Indian Institute of Science Education and Research Pune
Dr. Homi Bhabha Road,
Pashan, Pune 411008, INDIA.

April, 2023

Supervisor: Dr. Sandro Mereghetti

Certificate

This is to certify that this dissertation entitled Asymmetries in Surface Temperature Distribution of Neutron Stars towards the partial fulfilment of the BS-MS dual degree programme at the Indian Institute of Science Education and Research, Pune represents study/work carried out by Varun Shah at Indian Institute of Science Education and Research under the supervision of Dr. Sandro Mereghetti, Research Director, INAF-IASF Milano, Italy , during the academic year 2022-2023.

Dr. Sandro Mereghetti

Committee:

Dr. Sandro Mereghetti

Dr. Prasad Subramanian

This thesis is dedicated to my family, friends, and everyone else who has helped me reach where I am today.

Declaration

I hereby declare that the matter embodied in the report entitled Asymmetries in Surface Temperature Distribution of Neutron Stars are the results of the work carried out by me at the INAF-IASF Milano, Italy, Indian Institute of Science Education and Research, Pune, under the supervision of Dr. Sandro Mereghetti and the same has not been submitted elsewhere for any other degree.

Varun Shah

Acknowledgments

This thesis could not have been completed without the direct and indirect contributions of several people to whom I owe my gratitude. I hope this work reflects the role of their continuous support and guidance.

First, I would like to thank my Supervisor, Sandro Mereghetti, who accepted to guide me through this project. Thanks to him, I have not only developed a set of specialized skills but have gained the knowledge of what it is to be a good scientist, which I hope to make my own.

In particular, I owe gratitude to Dr. Michela Rigoselli who provided the observational data which is used to compare with my model. I thank Dr. Davide De Grandis for all the help he provided in the development of the ray-tracing software, suggestions about conducting the population study, and the very patient explanations of the magneto-thermal evolution of neutron stars. I thank Dominik Pacholski for his help in fixing my programs and for buying me coffee when I run out of coins. I have learned a lot from each of them.

I thank all my friends in Milano who were there for me during the ups and downs of this journey. I thank my friends at IISER-Pune with whom I shared four years of undergraduate enjoying life (and learning a few things every now and then). Their support was instrumental in the completion of this thesis.

In the end, I thank my family for their unwavering support throughout the duration of this project and before. I thank them for paving a path that allowed me to make the choice of studying what I love.

Abstract

Neutron stars are the final stage of the evolution of massive stars. They are formed when the core collapse of progenitor stars is halted by the degeneracy pressure of neutrons. As such, neutron stars have densities comparable to atomic nuclei, making them the densest objects with a surface known in the Universe. Neutron stars are born strongly magnetized ($\sim 10^8 - 10^{15}$G) and extremely hot($\sim 10^{11}$K). Predominantly identified by their pulsed radio emission, thermal emission from the stellar surface of a cooling neutron star is detected in soft x-rays from several sources. The thermal emission is directly affected by various physical properties of the star, and hence, carries a wealth of information bearing directly on the stellar age, radius, mass, composition, and magnetic field structure. The shape of the pulse profiles is principally dependent on the thermal map of the stellar surface and the viewing geometry. Observations of asymmetric and multi-peaked pulse profiles from several sources hint to the presence of an anisotropic surface thermal map. The thermal map is determined by the stellar magnetic field topology. A study of asymmetric pulse profiles helps understand any deviations from the generally accepted dipolar magnetic field structure of neutron stars.

This thesis investigates the model of neutron stars with a non-dipolar magnetic field topology where the second pole is shifted from the antipodal position (distorted-dipole). Using a general relativistic ray tracing software, populations of pulse profiles are generated with random viewing geometries and different temperature maps corresponding to the distorted-dipole field structure. Distributions of specific parameters that describe the anisotropies introduced in the thermal maps are compared with those of the observed sample of thermally emitting, isolated neutron stars from which x-ray pulsations have been detected (34 sources). Similar population studies have been performed for magnetars, the results of which are recreated in the thesis. Multiple studies that consider complex magnetic field structures to recreate asymmetric pulse profiles from thermally emitting sources have been done in the past for specific sources. These studies provide very broad conclusions as the shape of the pulse profile is affected by a variety of parameters. The novelty and relevance of this thesis is that it performs a general population study of specific parameters for a variety of randomized initial conditions which allows us to make more general and robust conclusions.

Contents

List of Figures

List of Tables

Introduction

Neutron stars are the remnants of the core of massive stars that underwent supernova explosions. Stars that are too small to ultimately collapse into a black hole, but massive enough to overcome the electron degeneracy pressure that supports white dwarfs, create neutron stars. As a result, neutron stars are held together by neutron degeneracy pressure and host extreme environments (high density, strong magnetization, high temperatures, and fast spin). The timing and spectral study of their emission ranging from radio frequencies to gamma rays, allow us to study physics in extreme conditions that can not be recreated on the Earth.

Even before their discovery in 1967, neutron stars were predicted to be powerful sources of x-ray emission, owing to their extremely high surface temperature ($\sim 10^6$K) [9]. The x-ray emission from isolated neutron stars generally consists of two distinct components: non-thermal radiation due to charged particles accelerated in the magnetosphere and thermal radiation from the hot surface. Observations of middle-aged isolated neutron stars in the soft x-ray band (0.2-4 keV) show the pulse profiles dominated by the thermal emission. The magnetic field structure, internal composition, and the presence of an atmosphere determine the surface thermal properties as a function of the star age. The observed thermal flux is affected by the viewing geometry, the mass of the star, and the properties of the stellar atmosphere. Timing studies of the thermal pulse profiles allow us to directly probe the stellar thermal structure, atmospheric composition, magnetic field structure, and calculate bounds for the mass and radius of the star.

The problem of calculating pulse profiles given a surface thermal map for a dipolar field was first tackled by Page(1995) [23]. Page [23] showed that for a symmetric thermal map

resulting from the presence of a dipolar field, the pulse profiles are always symmetric[1] with a small pulse fraction ($< 10\%$). The simple dipolar model fails to explain the asymmetric profiles with large pulse fractions that are often observed. Zane and Turolla(2006)[33] obtained fits for the asymmetric profiles for the so-called 'magnificent seven', a class of thermally emitting isolated neutron stars, using a star-centered dipole plus a quadrupolar field. This magnetic field topology is not entirely realistic. However, this investigation provides a strong hint that the field topology of neutron stars is not just a simple dipole. Geppert, Kuker, and Page(2005,2006)[13][25] explored cases considering a poloidal crustal field with a toroidal component that gives rise to polar caps of different sizes which explains the observations of double-peaked profiles with different peak heights.

In this context, there is strong evidence that the magnetic field topology of neutron stars deviates from the simple and generally assumed dipolar structure. The shape of the pulse profiles is strongly dependent on the surface thermal map and viewing geometry. Instead of recreating the profiles of individual sources, a study of specific parameters that target certain anisotropies in the surface thermal map for a population of simulated pulse profiles generated for random viewing geometries and comparison with observed data provides more general conclusions about the thermal structure of the stellar surface.

In this thesis, I describe the development of a general-relativistic ray-tracing code to compute the expected pulse profiles of neutron stars for any viewing geometry, GR factor, beaming function, and thermal map. The program is used to create populations of pulse profiles for various values of the determining parameters for a 'deviated-dipole' thermal map. The properties of the pulse profiles obtained from these populations are compared with the data from thirty-four thermally emitting neutron stars. This is done by characterizing the profiles with a set of parameters, whose distributions are then compared with the observed ones. The material is organized as follows: in Chapter 1 the basic physics of neutron stars is reviewed; Chapter 2 explains the development of the ray-tracing code and the parameters under consideration; Chapter 3 covers the population study methodology with an example; the observed data are described in Chapter 4; Chapter 5 is devoted to the results obtained from the entire study; and the conclusions follow in Chapter 6.

[1]Symmetric profiles are profiles that remain same when flipped about a critical phase angle. In this thesis, asymmetric pulse profiles refer to single-peaked profiles that are skewed to one side, double-peaked profiles where the peaks have unequal heights, and double-peaked profiles where the phase difference between the two peaks is less than π. Profiles with more than two peaks are termed 'complex-structured' profiles.

Chapter 1

Neutron Stars

1.1 Historical Introduction

The development of the idea of neutron stars took place in the early 1930s following several vital discoveries in fundamental physics. In 1930, Subramanyan Chandrashekhar showed that the collapsed stellar core weighing more than 1.4 solar mass could not be stably held by electron-degeneracy pressure and would continue to collapse under extreme gravitational force[8]. The discovery of the neutron by James Chadwick in 1932[7] led scientists to theorize a star composed entirely of neutrons. The upper limit to the mass of such objects was derived by Robert Oppenheimer and George Volkoff in 1939[21] using the earlier work of Richard Tolman[29] (Tolman-Oppenheimer-Volkoff limit). Walter Baade and Fritz Zwicky hypothesized the formation of Neutron Stars as a result of supernova explosions in 1934[2]. However, Neutron stars remained objects of imagination until advancements in x-ray and Radio astronomy led to their first observations in the 1960s.

Experiments done by the Naval Research Lab in the 1950s showed very faint x-ray emission from the solar corona which led astronomers to believe that x-ray emission from Neutron Stars would be too faint to be visible. However, x-rays from Sco X-1, a source in the constellation Scorpio, later identified as a neutron star, were observed by Bruno Rossi and Riccardo Giacconi in 1962[14]. Similar observations were made for the Crab supernova remnant. These observations were not sensitive enough to definitively identify these sources as Neutron Stars.

The seminal discovery of radio pulses by Jocelyn Bell in 1967[16] was the first observation confirming the existence of pulsars. The link between the radio pulses and Neutron Stars was provided by Franco Pacini[22] and Thomas Gold[15] with their work on rapidly rotating, highly magnetized neutron stars that emit radiation in radio wavelengths at the expense of their rotational energy. This discovery was quickly followed by the discovery of the pulsar in the Crab nebula and the Vela supernova remnant.

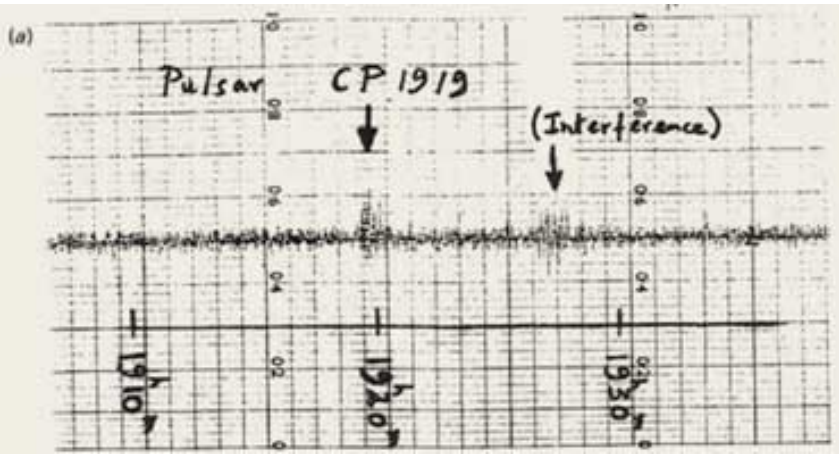

Figure 1.1: The first detection of a pulsar by Jocelyn Bell at Cambridge University in 1967. The figure is taken from `https://www.cam.ac.uk/stories/journeysofdiscovery-pulsars`, where a detailed account of Bell's role and the controversy around the recognition is given.

Over the years many radio pulsars have been discovered (now counting more than 3000). Radio emission due to magnetic braking and field decay can not describe all the pulsar activity. Despite the fact that pulsars have been observed for over half a century, the exact mechanisms leading to the production of radio emission are not yet known. The Einstein X-ray Observatory, ROSAT, and EXOSAT provided the first observations of Neutron Stars at high energies. Modern telescopes like Chandra and XMM-Newton provide outstanding imaging capability and spectral sensitivity. The study of pulsar activity has been greatly extended by the increased range of spectrum in which they can be observed by modern telescopes. Two main classes of models: the polar cap and the outer gap have been proposed to explain the HE emission. In both models, the high-energy photons are emitted by curvature radiation (CR), Synchrotron radiation (SR), and Inverse-Compton scattering (ICS).
Owing to their precise timing properties, pulsars are being used in pulsar timing arrays (PTAs) to detect gravitational waves. Neutron stars are emitters of neutrinos and are the

targets of neutrino telescopes. Pulsars act as laboratories to study physics in high-energy, high-density, high-$\vec{B}$ environments that can not be replicated on the Earth. They emit in a broad range in the electro-magnetic spectrum and are observable by GW and neutrino detectors. In this way, pulsars play a vital role in multi-messenger astronomy.

1.2 NS formation and Structure

Massive stars of the order of 8-30$M_{\odot}$ die in core-collapse supernova explosions. In these stars, the stellar core with mass greater than the Chandrashekhar limit, i.e. 1.4 $M_{\odot}$, can not be stably held by the electron degeneracy pressure when the nuclear fuel is exhausted. The iron core grows until electron capture (degenerate electrons captured by protons to produce neutrons define an energetically advantageous state) or photodisintegration of heavy nuclei triggers the gravitational collapse. The gravitational binding energy released by the core collapse powers the supernova explosion. The core continues to collapse until nuclear density is reached, which in turn provokes a 'bounce' of the infalling material. The shockwave propagates outwards and leaves behind a hot, lepton-rich proto-neutron star.

The magnetic field in a collapsing star gets amplified by several orders of magnitude due to the conservation of magnetic flux. The magnetic decay timescale is much shorter than the collapse timescale for a length-scale of the magnetic field comparable to the stellar radius as the conductivity of the plasma inside the star is extremely high. Thus the field can be considered to be 'frozen-in' and the flux is conserved during the collapse. The field strength for 'frozen-in' fields increases as $B \propto \rho^{2/3}$, where ρ is the density. Assuming that the field strength in the core of massive stars is of the order of $\sim 10^9 G$, similar to strongly magnetized white dwarfs, the field strength of the neutron stars at the end of core-collapse would be of the order of $\sim 10^{13} - 10^{14} G$. This is comparable to the field strength observed (or estimated/measured) in young radio pulsars.

Neutron stars are born hot with a temperature of tens of MeV and with a short rotation period, as they spin up during the core collapse due to the conservation of angular momentum. Neutron stars cool over millions of years by neutrino losses until they reach a stable state with a temperature of the order of one MeV. The neutron stars continue to cool by thermal emission and slowly spin down due to magnetic braking.

A spherical structure is a good approximation for the star except for the cases with ultra-strong magnetic fields ($\geq 10^{17}G$) or ultra-short rotation periods (lower than a millisecond). The mechanical structure of a spherically symmetric star is described by the Tolman-Oppenheimer-Volkoff equation:

$$\frac{dP}{dr} = \frac{-GM_r\rho}{r^2}\left(1+\frac{P}{\rho c^2}\right)\left(1+\frac{4\pi r^3 P}{M_r c^2}\right)\left(1-\frac{2GM_r}{rc^2}\right)^{-1}$$

where r is the radial coordinate measured from the stellar center, M_r is the stellar mass inside a radius r, P is the pressure, ρ is the gravitational mass density, G is the gravitational constant and c is the speed of light.

The inner core can exist in massive neutron stars with $M \geq M_\odot$. It occupies the central part with $\rho \geq 2\rho_0$, where $\rho_0 = 2.8 \times 10^{14} g\ cm^{-3}$ is the nuclear saturation density. The composition of this region is uncertain.

The outer core has a mass densiy $0.5\rho_0 \leq \rho \leq 2\rho_0$. It is several kilometers thick and contains most of the stellar mass. It is mainly composed of neutrons and a mixture of protons and leptons.

The stellar crust and ocean contain electrons, and nuclei made of neutrons and protons. In the crust, which is about one kilometer thick, the nuclei are arranged in a crystalline lattice, and in the ocean, they form a liquid. With increasing density, nuclei become progressively neutron-rich due to the beta-captures that are favored by the increase of pressure of the degenerate electrons.

1.3 $P\dot{P}$ diagram and the NS zoo

A pulsar is characterized by its quick rotation and strong magnetization. Thus, a pulsar presents an accelerated electromagnetic field that radiates energy. Considering the classical model of a neutron star with a purely dipolar magnetic field with a moment $\mathbf{m}$; the energy emitted is given by the Larmor formula:

$$\dot{E} = \frac{-2}{3c^2}\ddot{\mathbf{m}}^2 = \frac{-B_d^2 R^6}{6c^3}\Omega^3 \sin^2\alpha$$

Where B_d is the field strength at the poles, R is the radius of the neutron star, Ω is the angular velocity, and α is the angle between the rotation and magnetic axis. The dot denotes the time derivative and c is the speed of light.
The energy radiated depends on the angular velocity, thus, the neutron star loses rotational kinetic energy as it spins down. The loss of kinetic energy can be expressed as: $\dot{E}_{rot} = I\Omega\dot{\Omega}$. I is the moment of inertia of the neutron star (for typical values, I=10^{45} g cm^2). Assuming that B_d, R, and I are constants and that $\Omega(0) >> \Omega(t)$, we can equate the two energy loss equations and integrate over time to get:

$$\tau = \frac{-1}{2}\frac{\Omega}{\dot{\Omega}} = \frac{1}{2}\frac{P}{\dot{P}}$$

$P = 2\pi/\Omega$ is the period of rotation that can be directly measured. This expression defines the **characteristic age** of a neutron star.
Using the spin period and its time derivative, the field strength at the pole can be expressed as:

$$B_d = \sqrt{\frac{6Ic^3}{4\pi^2 R^6 \sin^2\alpha} P\dot{P}} \simeq 3.2 \times 10^{19}\sqrt{P\dot{P}} \quad G$$

the numerical value has been calculated for the characteristic values $I \simeq 10^{45} gcm^2$, $R \simeq 10$ km , $\sin\alpha \simeq 1$ and P measured in seconds. This is the spin-down field that gives a first estimate of the magnetization of a neutron star. The spin period (P) and the time derivative of the period ($\dot{P}$) can be used to estimate the age and magnetization of pulsars.

Similarly to the HR diagram in stellar astronomy, the $P\dot{P}$ diagram is a useful tool to represent and classify neutron stars and understand their evolution. Different classes of pulsars can be found in different regions of the $P\dot{P}$ diagram. The major classes are as follows:

Radio pulsars fill the central region of the diagram. They have typical periods of $0.1 - 1$ seconds and fields of the order of $\simeq 10^{12} G$. They are noted for pulsations in radio wavelengths but are also visible in x-ray and γ- ray bands. The radio emission is powered by the rotational energy of the star. Charged particles extracted from the stellar surface are accelerated by the electric voltage gap created by the co-rotating magnetic field. The photons of the curvature radiation from the charged particles are converted into electron-positron

pairs in the high magnetic field that leads to a pair cascade and results in the coherent radio-emission observed [26].

MSPs are millisecond pulsars. They are found in the bottom-left part of the diagram which corresponds to short periods and low field ($\simeq 10^{8-10}G$). These pulsars are a by-product of the recycling scenario. As a neutron star ages, it spins down, and its magnetic field decays. Old pulsars in binary system that experience a long period of accretion (by Roche-lobe overflow from the companion star) spin up to millisecond periods and their field gets buried by the accreted material. These pulsars are often termed recycled pulsars [19].

Magnetars are found in the top-right region of the diagram which corresponds to young age ($\simeq 1--100kyr$) and strong field ($\simeq 10^{13-15}G$). Magnetars are the most variable sources in different classes of isolated neutron stars. They are characterized by bright emission in the x-ray and soft γ-ray band. They show transient activity like outburst periods and high-energy bursts that often reach super-Eddington luminosities [20].

RRATs, or rotating radio transients, sporadically emit radio pulsar-like signals. They are discovered in single-pulses but not in periodicity-based searches. Field and age estimates can be derived from this irregular periodicity [6].

CCOs, or compact central objects, are X-ray sources found at the centre of supernova remnants. They have a low magnetic field ($\leq 10^{11}G$) as abundant accretion in the post-supernova stage buries the field in the crust. A consequence of this is the anisotropy in the surface thermal distribution [32].

XINs stands for x-ray isolated neutron stars. These objects do not show radio emission but exhibit only thermal x-ray emission. So far, seven such objects are known and they are nicknamed 'The magnificent seven'. The proper motion of these sources is too fast for them to be powered by accretion from the interstellar medium. These sources show no evidence of being associated with a supernova remnant or having a binary companion. The steady x-ray flux and a high x-ray to optical flux ratio makes them useful to study the mass-radius relationship, spectral, and timing study of their pulse profiles [3].

1.4 Observing Pulsars

Historically and to this day, radio emission is the main mechanism through which most pulsars are observed. The ATNF pulsar catalog (`https://www.atnf.csiro.au/research/pulsar/psrcat/`) presently contains 3389 identified pulsars, thousands of which were observed by radio telescopes all over the world in the past few decades. Apart from the radio emission due to magnetic braking, the exact mechanisms behind radio emission are still poorly understood. This theoretical problem creates difficulties in the interpretation of new data.

Pulsars also emit in the high-energy region of the electromagnetic spectrum through various mechanisms. Their x-ray emission is widely studied by telescopes like Chandra, XMM Newton, INTEGRAL, NICER, and several others. The x-ray emission from pulsars is attributed to various thermal and non-thermal mechanisms such as the following:

- Non-thermal emission from charged, relativistic particles that are accelerated in the pulsar magnetosphere. The flux is directly dependent on the density of high-energy, radiating electrons independent of the radiation mechanisms (synchrotron radiation, curvature radiation, or inverse Compton scattering). The energy distribution of the charged particles follows a power law, thus, the spectra of this radiation are also characterized by a power law. Emission from these accelerated charged particles can be seen from optical to gamma frequencies.

- Non-thermal emission from pulsar-driven synchrotron nebulae. Rotating pulsars produce a relativistic, magnetized wind composed mainly of electrons and positrons that get confined by the surrounding medium. Synchrotron and IC emission due to the interaction of these relativistic particles with ambient magnetic and photonic fields produces radiation from radio to gamma frequencies.

- Thermal emission in x-rays from the neutron star polar caps that are heated by the bombardment of relativistic, charged particles streaming in along the open field lines from the pulsar magnetosphere.

- Thermal emission from the hot surface of a cooling neutron star. The surface thermal emission shows flux variation in accordance with the pulsar rotation period and a smooth thermal spectrum which can be in a first approximation described by a blackbody.

Neutron stars are also observed at very high energies in gamma rays. The discovery of radio-quiet pulsars that can be observed only in gamma or x-rays led to the development of theories describing different emission geometry at different energy bands. The emission of gamma rays is generally described by two emission models: the polar cap model and the outer gap model. The polar cap model puts the emission zones in the vicinity of the magnetic poles. The gamma-ray emission forms a cone centered at the poles and yields a pulse profile that is single or double-peaked depending on the viewing geometry. The outer gap model assumes the emission zones to be near the light cylinder of the pulsar. This model does not face the problem of one-photon pair creation in the presence of extremely strong magnetic fields ($\gamma + B \longrightarrow e^+ + e^-$). In both models, the high-energy radiation is emitted by relativistic particles accelerated in the very strong electric field generated by the magnetic field co-rotating with the neutron star. These particles are generated in cascade (avalanche) processes in charge-free gaps, located either above the magnetic poles or close to the light cylinder. The main photon emission mechanisms are synchrotron or curvature radiation and inverse Compton scattering of soft thermal x-ray photons emitted from the hot neutron star surface.

Pulsars act as precise cosmic clocks due to their extraordinary timing consistency. This property is exploited by pulsar timing arrays to detect gravitational waves and by traditional gravitational wave detectors to study general relativity in the strong-field environment. Pulsars play an important role in the field of multi-messenger astronomy. The merger of two neutron stars gave rise to the first multi-messenger event GW-GRB 170817 which was studied by the LIGO-VIRGO collaboration with several other telescopes in the electromagnetic wavelengths. BH-NS and NS-NS mergers are at the center of the work done by gravitational wave detectors all over the world. Observation of continuous gravitational waves from deformed neutron stars is a goal of GW detectors. Neutron stars are also sources of copious neutrino emission and observing this is a future target of the ICECUBE neutrino telescope.

1.5 Thermal Emission

A neutron star is born hot ($\sim 10^{11} K$), but only after a few days of its birth, its temperature drops to the order of $\sim 10^9 K$ due to neutrino emission. It subsequently proceeds to cool down by neutrino cooling and thermal emission. The neutrino cooling era lasts $\sim 10^5$ years,

after which photon cooling takes over. The surface thermal distribution is dependent on the heat transport from the core, the magnetic field structure and strength, and the properties and composition of the various regions of the star. The following discussion is from [24].

1.5.1 Heat transport and Thermal evolution

The heat transport and thermal evolution equations can be solved to determine the thermal structure of the neutron star.

$$c_v e^{\phi} \frac{\partial T}{\partial t} + \nabla \cdot (e^{2\phi} F) = e^{2\phi}(H - Q_v); \quad F = e^{-\phi} \hat{\kappa} \cdot \nabla (e^{\phi} T)$$

where F is the heat flux density, H is the heating power per unit volume, c_v is specific heat, Q_v is neutrino emissivity, and $\hat{\kappa}$ is the thermal conductivity tensor.

The inner boundary condition to the system of equations is $F = 0$ at $r = 0$. The outer boundary condition is determined by the properties of a heat-blanketing envelope, which serves as a mediator of the internal heat into the outgoing thermal radiation. For weak magnetic fields, the 1-D solution to the heat transport and the thermal evolution equations yields essentially radial temperature gradients. 2-D solutions considering strong magnetic fields explain the non-uniform thermal distribution over the stellar surface.

The specific heat (c_v) is dominated by two components: electron gas and ions. In the neutron star crust, the electrons form a Fermi gas and their contribution to heat capacity per unit volume is given as:

$$c_{v,e} = \frac{\rho_{Fe}^2 T}{3c\hbar^3} = n_e \frac{\pi^2 T}{c\rho_{Fe}}.$$

Electrons are the primary heat conductors in the crust and photons in the atmosphere. The net thermal conductivity is obtained by summing its radiative and electron components ($\kappa = \kappa_e + \kappa_r$). $\kappa = anT/m\nu$ where a is a numerical coefficient ($a = 3/2$ for a non-degenerate gas and $a = \pi^2/3$ for degenerate particles), ν is the effective collision rate, m is the mass, and n is the number density.
In neutron star envelopes, $m = m_e\sqrt{1 + x_r^2}$ and $\nu = \nu_e$ is determined by the electron-ion and electron-electron Coulomb collisions. $x_r = \rho_f/m_e c$ is the relativistic factor, $\rho_f = \hbar k_f$ is

the Fermi momentum, and $k_f = (3\pi^2 n_e)^{1/3}$ is the Fermi wave vector [10]. In the crystalline phase, electron-ion scattering is described as phonon scattering. According to Mathissen's rule, $\nu_e = \nu_{ei} + \nu_{ee}$ where ν_{ei} and ν_{ee} are effective scattering frequencies of electron-ion and electron-electron collisions. Electron heat conduction in the stellar crust determines the final thermal luminosity of the star.

1.5.2 Effect of Magnetic Field

The dimensionless ratio of electron cyclotron energy to the atomic unit of energy, electron rest energy, and temperature are used to conveniently characterize magnetic fields in a plasma:

$$\gamma = \frac{B\hbar^3}{m_e^2 ce^3} = \frac{B}{B_0}; \quad b = \frac{\hbar eB}{m_e^2 c^3} = \frac{B}{B_{QED}}; \quad \zeta_e = 134.34\frac{B_{12}}{T_6}$$

where $\omega_c = eB/m_e c$ is the electron cyclotron frequency, $B_0 = 2.3505 \times 10^9 G$ is the atomic unit of magnetic field, $B_{QED} = 4.414 \times 10^{13} G$ is the critical magnetic field in Quantum-Electrodynamics, $T_6 = T/10^6$K, and $B_{12} = B/10^{12}$G. The motion of charged particles in a magnetic field is quantized in discrete Landau levels. the kinetic energy ϵ of an electron at the Landau level N depends on its longitudinal momentum p_z as:

$$\epsilon_N(p_z) = c(m_e^2 c^2 + 2\hbar\omega_c m_e N + p_z^2)^{0.5} - m_e c^2$$

The Landau quantization becomes important when the electron cyclotron energy is at least comparable to both the electron Fermi energy and temperature T.
The strong magnetic fields affect the heat conductivity of both photons and electrons. The heat conductivity κ depends on the opacity χ as:

$$\kappa = \frac{16\sigma_{SB} T^3}{3\rho\chi}$$

where σ_{SB} is the Stefan-Boltzmann constant. The effective opacities for transport parallel

and perpendicular to the field are given as:

$$(\chi^{\parallel}_{\omega,j})^{-1} = \frac{3}{4}\int_0^{\pi} 2cos^2(\theta_B)\frac{sin(\theta_B)d\theta_B}{\chi_{\omega,j}(\theta_B)}$$

$$(\chi^{\perp}_{\omega,j})^{-1} = \frac{3}{4}\int_0^{\pi} sin^2(\theta_B)\frac{sin(\theta_B)d\theta_B}{\chi_{\omega,j}(\theta_B)}$$

where θ_B is the angle between the wave vector and the local field line. In deep, strongly magnetized photospheres, Thompson scattering dominates and in other cases, free-free absorption prevails.

The electron heat conduction in the crust is affected by the magnetic field if the Hall magnetization parameter is large.

$$\omega_g\tau = 1760\frac{B_{12}}{\sqrt{1+x_r^2}}\frac{\tau}{10^{-16}s}$$

where $\omega_g = \omega_c/\sqrt{1+x_r^2}$ is the electron gyro-frequency, and τ is the effective relaxation time. In a quantizing magnetic field, the mean free times parallel and perpendicular to the field are given as:

$$\tau_{zz} = \tau_{\parallel}; \tau_{xx} = \frac{\tau_{\perp}}{1+(\omega_g\tau_{\perp})^2}; \tau_{yx} = \frac{\omega_g\tau_{\perp}^2}{1+(\omega_g\tau_{\perp})^2}$$

Figure 1.4 shows the electron thermal conductivity for different field strengths and temperatures. Thermal conduction is facilitated along the field lines thus the final temperature distribution on the surface is determined by the magnetic field structure.

1.5.3 Blanketing Envelope

The effective surface temperature T_s at every boundary temperature T_b depends on the properties of the blanketing envelope. For most neutron stars except for the hottest ones, the neutrino energy loss in the blanketing envelope is negligible. Thus, the fluxes F_b and F_s are equivalent. It is sufficient to know the $T_b - T_s$ relation to understand the final thermal map. The heat transport is facilitated if the envelope is composed of light elements as the

collision frequencies ν_{ei} are higher for high-Z elements, thus, their conductivity is lower. The 1D approximation overestimates the blanketing effect as it does not consider non-radial heat transport in regions where the field is nearly parallel to the surface. A 2D treatment is required for a dipolar or complex structured magnetic field.

Figure 1.5 shows the 1-D and 2-D solutions to the heat transport equations for a dipolar magnetic field yielding a $T_b - T_s$ relation.

The thermal conduction in a spherically symmetric star occurs through different transport mechanisms in its different layers. The electron heat conduction is principally responsible for the thermal structure of the crust. Above a certain limit, the magnetic field affects electron heat transport and yields anisotropic surface temperature distributions.

1.5.4 Thermal x-rays from cooling neutron stars

Neutron stars lose their excess lepton content seconds after their birth. At the end of the residual contraction, they become completely transparent to neutrinos. In the initial cooling stages, the crust is hotter than the core as the core cools rapidly through copious neutrino emission. After 10-100 years, the cooling wave reaches the surface, thereafter, the star cools in a quasistationary way. There are two phases of quasistationary cooling: the neutrino cooling stage lasts for $\sim 10^5$ years during which the core cools via neutrino emission, photon cooling stage begins when the low temperature of the core makes the neutrino energy losses smaller than the losses due to electromagnetic radiation from the surface.

Over the course of its evolution, some patches of the stellar surface can also heat up by external processes like the bombardment of the polar caps by charged particles streaming in along the open field lines, or by internal processes like the dissipation of a strong magnetic field. The age of an observed source can be estimated by its period and period decay (see section 1.3). Using the calculated age and the effective luminosity, cooling curves that trace the thermal evolution of cooling neutron stars assuming different field strengths and blanketing envelope composition can be made as shown in the following figure.

As $T_s \approx 10^6\,\mathrm{K}$, thermal emission is in the soft x-rays. The magnetospheric emission from neutron stars is generally in hard x-rays and the thermal emission is in soft x-rays. In young pulsars, the non-thermal emission is much brighter than the thermal emission which makes it impossible to identify the thermal x-rays. Old neutron stars are not sufficiently bright in x-rays due to continued cooling. The thermal emission in x-rays dominates over the non-thermal emission in middle-aged neutron stars, thus, observing middle-aged, isolated neutron stars in x-rays allows us to study their thermal emission. As thermal emission is dependent on several factors of the star's physical properties, it opens further avenues to study those.

The red-shifted quantities observed by a distant observer as calculated by e.g. Thorne(1977)[28] are

$$R^\infty = R/\sqrt{1-r_g/R}; T^\infty_{eff} = T_{eff}\sqrt{1-r_g/R}; L^\infty_{ph} = L_{ph}(1-r_g/R)$$

where $4\pi\sigma_{SB}R^2T^4_{eff} = L_{ph} = \int F_{ph}d\Sigma = \sigma_{SB}\int T^4_s d\Sigma$, F_{ph} is the local flux density, and $d\Sigma$ is the surface element.

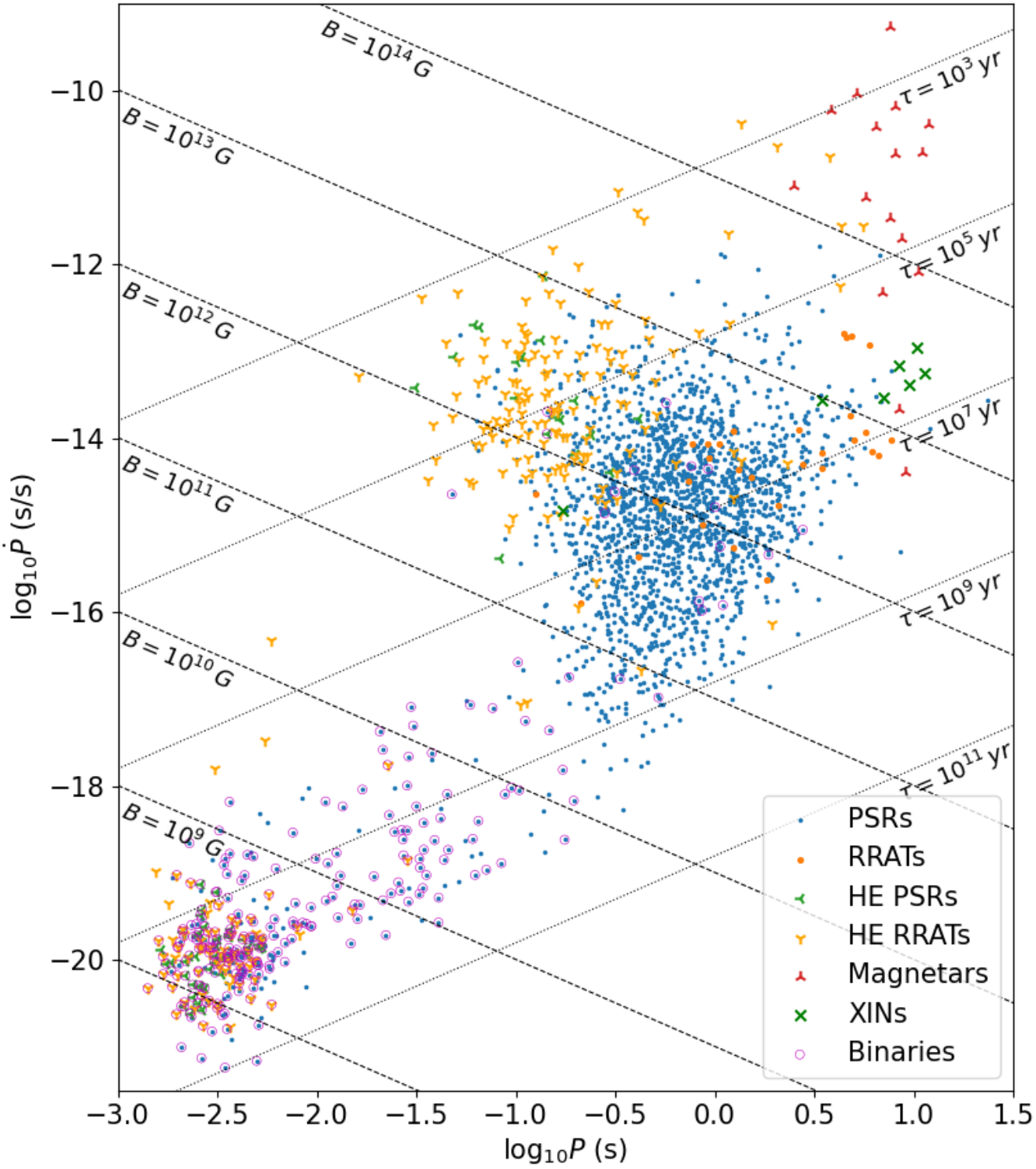

Figure 1.2: The $P\dot{P}$ for the known pulsars is created using the data from `https://www.atnf.csiro.au/research/pulsar/psrcat/`. The labels refer to the class of pulsars (PSRs = radio pulsars, RRATs = rotating radio transients, HE = high energy, XINs = x-ray isolated neutron stars). The dotted and dashed lines are loci of constant characteristic age.

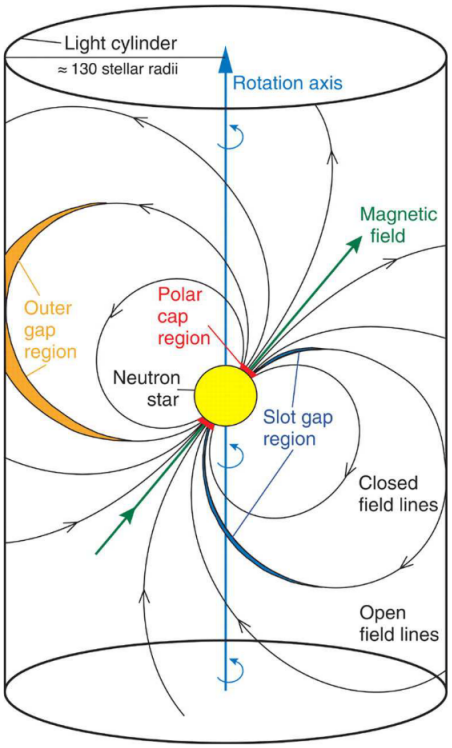

Figure 1.3: Schematic diagram describing the structure of pulsar field lines and the light cylinder. The polar cap model attributes HE emission to the vicinity of magnetic poles and the outer gap model assumes the emission zones to be near the light cylinder.

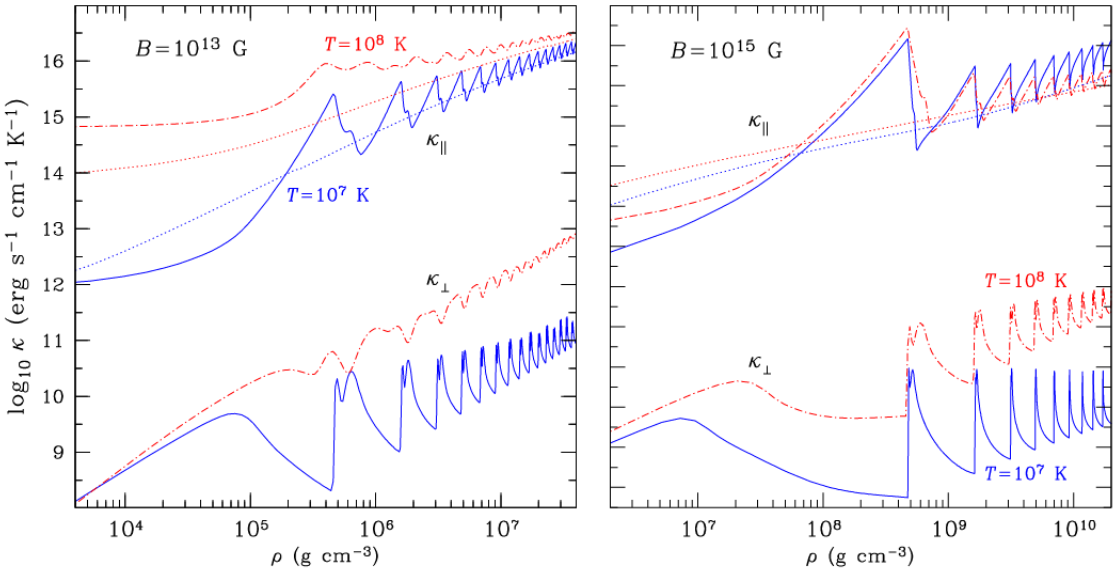

Figure 1.4: The mean free times of electron motion in the crust are dependent on the angle between the wave vector and the field lines. The plots show conductivity parallel and perpendicular to the magnetic field for different temperatures. For comparison, the non-magnetic thermal conductivities are shown by the dotted line. Figure is taken from [24].

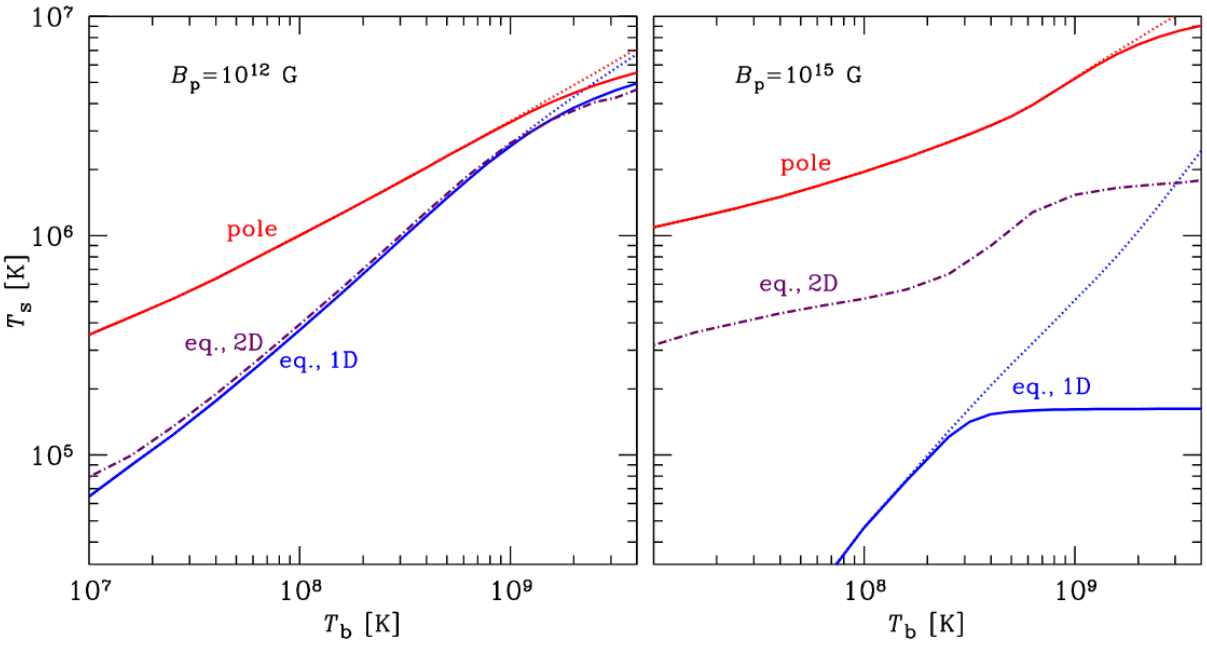

Figure 1.5: The plots show the local effective surface temperature T_s as function of the temperature T_b at the bottom of a heat blanketing envelope with $\rho_b = 1010 gcm^3$ for a neutron star with mass $M = 1.4 M\odot$, radius $R = 12.6$ km, and the dipole magnetic field with polar strength $B_p = 1012$ G (left panel) and 1015 G (rightpanel). The upper solid curve shows T_s at the magnetic pole, and the lower curve shows T_s at the equator. The dot-dashed curve shows the result of a full 2D calculation for T_s at the magnetic equator. The figure is taken from [24].

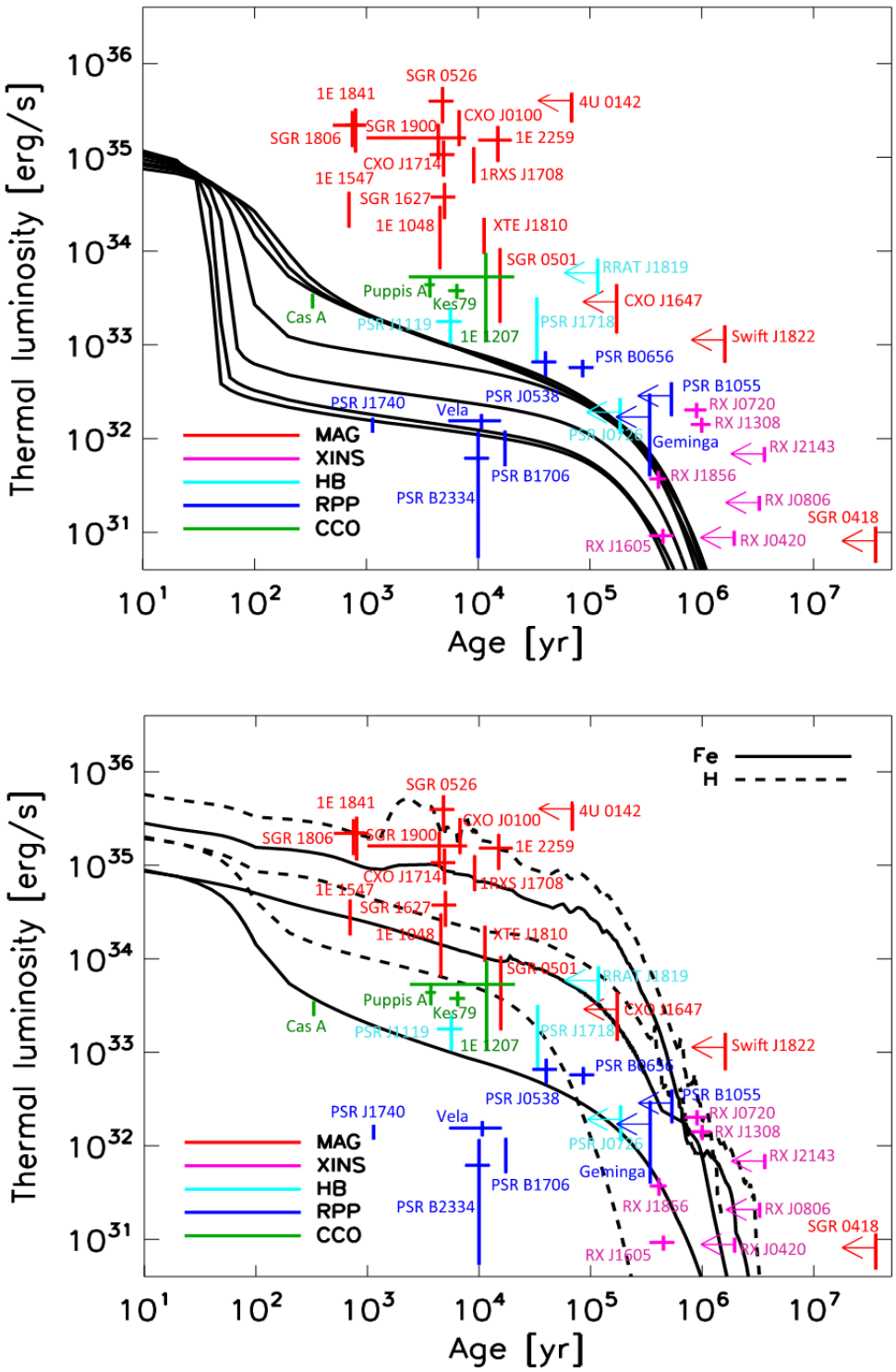

Figure 1.6: The figure shows the theoretical cooling curved plotted along with the observed data as generated by [31] and [24]. MAG=Magnetars and other abbreviations are as described in section 1.3. The solid lines in the upper panel correspond to cooling curves for stars with an iron envelope for different masses. The solid and dashed lines in the lower panel correspond to cooling curves for stars with iron and hydrogen envelopes respectively. The multiple lines are for different initial polar magnetic field strength.

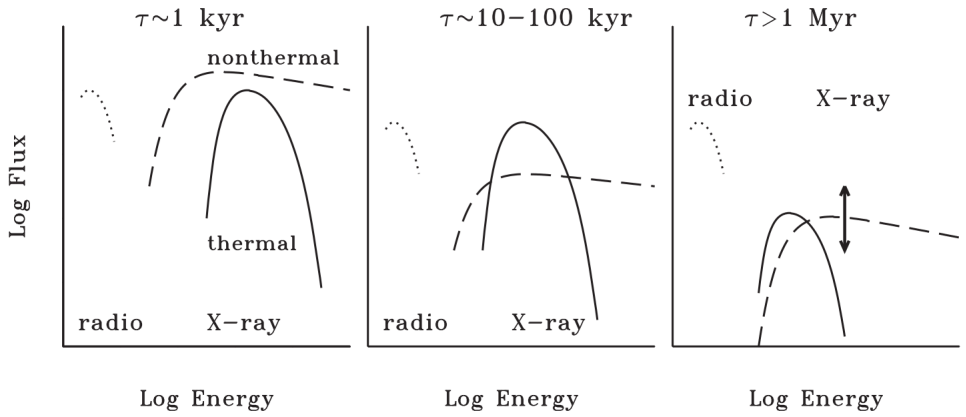

Figure 1.7: The figure illustrates what radiative component: thermal or non-thermal; dominates the x-ray flux for neutron stars of the age τ. The figure is taken from [3].

Chapter 2

General Relativistic Ray Tracing: Simulating Pulse Profiles

In this chapter, the physical parameters that affect the pulse profiles are described. First, the effects of gravitational light bending, the surface thermal map, and the beaming function are presented. The section regarding flux integration puts together all the factors and provides a description of how the ray tracing program is created. The model can be used to create pulse profiles given initial configurations for any viewing geometry.

2.1 General Relativistic Effects

The bending of photon trajectory due to gravity is a classical effect of general relativity. Weak bending gives rise to the phenomena of gravitational lensing and strong bending near compact objects (neutron stars and black holes) dominantly affects their observed emission properties.

The gravitational bending of the path of photons can be calculated using an approximate formula derived by Beloborodov(2002)[4]:

$$1 - cos(\alpha) = (1 - cos(\psi)) \left(1 - \frac{r_s}{R}\right)$$

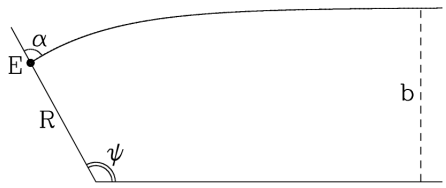

Figure 2.1: Gravitational light bending near the surface. E is the emission point, R is the radius of the neutron star, b is the impact parameter, and α is the emission angle. The bending angle β is equal to $(\psi - \alpha)$. The figure is taken from [4].

r_s is the Schwarzchild radius of the neutron star which is defined as $r_s = \frac{2GM}{c^2}$. The approximation holds with high accuracy at radii $R \geq 2r_s$.

The bending of light makes visible a surface area greater than a single hemisphere. The emission angle α can not exceed 90 degrees. The bound on angle α puts a bound on the angle ψ; thus the only factor determining the extent of the visible surface is the ratio of the Schwarzchild radius and the neutron star radius ($\frac{r_s}{R}$). This ratio is termed as the GR factor further on.
The increased visible surface area makes the pulsations less prominent and yields a lower value of the pulsed fraction, and for asymmetric (non-dipolar) surface thermal maps; depending on the viewing geometry, results in asymmetric or multi-peaked pulse profiles.
In this way, gravitational light bending is a crucial effect that affects the thermal emission from neutron stars.

2.2 Thermal Distribution

Electrons are the most important heat carriers in the neutron star crust. In the atmosphere, heat is principally carried by photons. The two heat transport mechanisms work simultaneously and the final heat conductivity(κ) can be expressed as $\kappa = \kappa_r + \kappa_e$, where κ_r and κ_e denote respectively the radiative and electron components of the heat conductivity[24]. The electron heat conduction is strongly affected by the strong magnetic field of the neutron star.

The surface thermal map or the surface intensity distribution depends on the local mag-

netic field strength and the angle it makes with the radial direction(ψ') at any point. As approximated by Heyl and Hernquist(1998)[17], the flux emerging from a point on the stellar surface is $\sim B^m cos^2(\psi')$ with $m = 0.4$. For a dipolar field structure, the following distribution as used by DeDeo, Psaltis, and Narayan(2001)[12] can be used:

$$I_0(\theta_m, \phi_m) \sim I_0 \frac{cos^2\theta_m}{(3cos^2\theta_m + 1)^{0.8}}$$

Where θ_m is the magnetic co-latitude and ϕ_m is the magnetic longitude. Increasing the exponent of the cosine makes the brighter polar caps more concentrated.

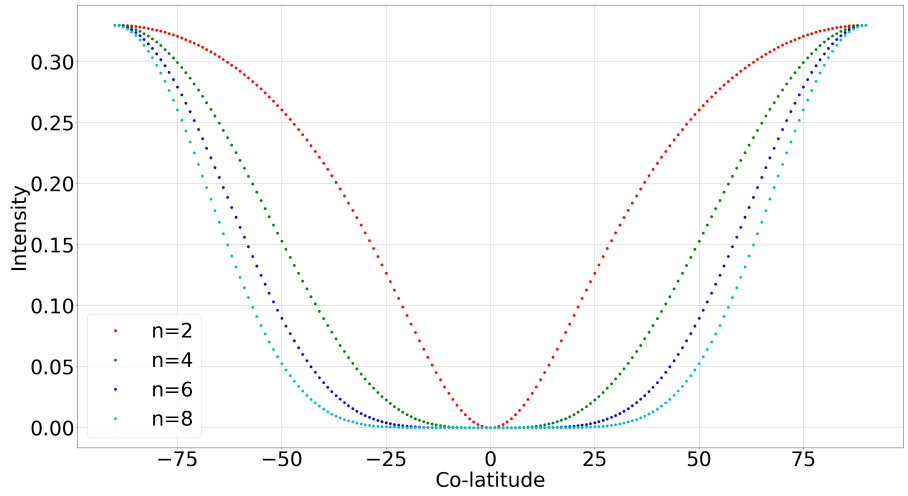

Figure 2.2: Surface intensity vs magnetic co-latitude (in degrees).

To explore the cases with an asymmetric surface thermal map, a different intensity function must be used.

The two parameters that introduce anisotropy in the thermal distribution are: the deviation angle of the secondary pole from the antipodal position (ζ) and the intensity ratio of the two poles (R).
A Gaussian intensity distribution centered at each hot spot is assumed. The emission intensity at any point on the grid is calculated by adding the contribution from the Gaussian around each hot spot as follows.

$$I_0 = Re^{-(dP_1^2)} + e^{-(dP_2^2)}$$

Where, r is the intensity ratio, dP_1 is the angular distance of any point from the primary hot spot, and dP_2 is the angular distance from the secondary hot spot. The angular distance is calculated using the Haversine formula which determines the great-circle distance between any two points on a sphere using their latitudes and longitudes (in this case, the co-latitudes and longitudes):

$$a = sin^2(\Delta\phi/2) + cos(\phi_1)cos(\phi_2)sin^2(\Delta\lambda/2)$$

$$c = 2arctan(\sqrt{a}/\sqrt{(1-a)})$$

ϕ is the co-latitude, λ is the longitude, and c is the angular distance.

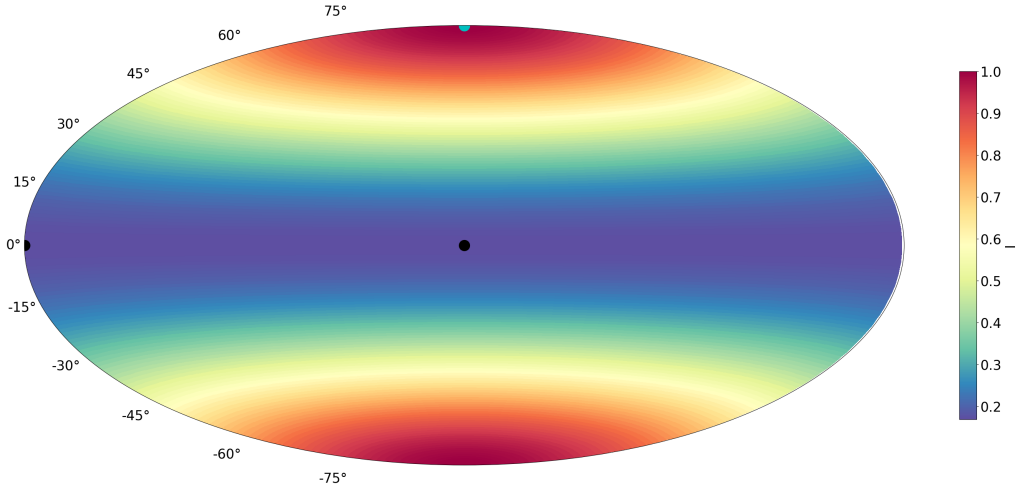

Figure 2.3: Thermal map of the antipodal case.

The emission from any point on the stellar surface is considered to be isotropic, i.e., the intensity distribution expression has no dependence on the angle of emission (θ'). Due to the relativistic effects, radiation must be emitted at a specific angle at any given point on the surface to reach the observer. This radiation has to travel through a thin atmosphere which significantly alters the radiation properties depending on the emission angle. The final intensity function describing the emission from the stellar surface depends on the magnetic field structure and the atmospheric properties of the neutron star as it incorporates the

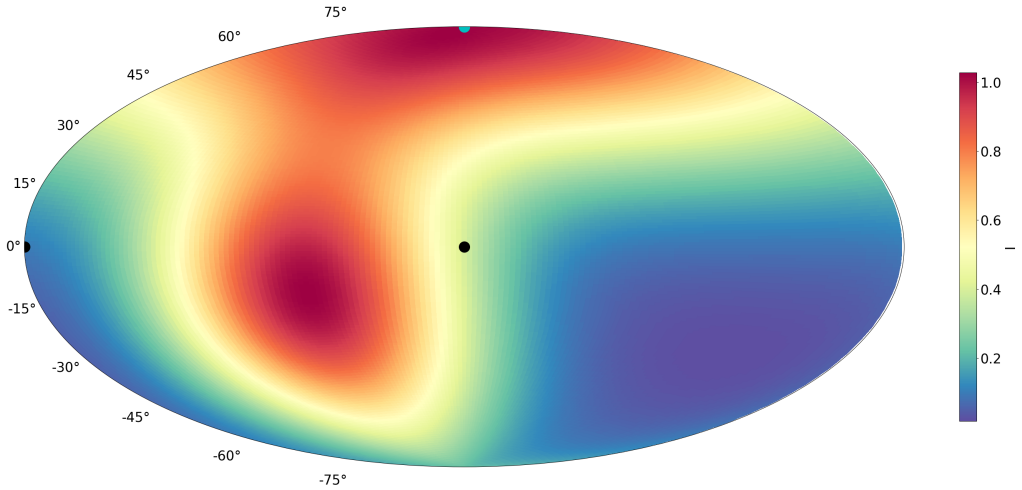

Figure 2.4: Thermal map of the neutron star surface with the secondary hot spot deviated by 70 degrees from the antipodal point along longitude = 120 degrees.

thermal map and the beaming function.

2.3 Beaming

The relativistic effect of the curved photon path affects the pulse amplitudes. A brightness distribution $I(\theta_m, \phi_m, \theta')$ is defined all over the surface of the star. θ_m and ϕ_m are the co-latitude and the longitude respectively (coordinates in the magnetic frame). θ' is the angle with respect to the surface normal at which the photon is emitted to reach the observer. The dependence of the emerging intensity on θ' is determined by the beaming function.

The beaming of surface thermal radiation from neutron stars depends on the physical properties and composition of the atmosphere present. Neutron star surface is covered by a thin atmosphere that can be in a plasma or a condensed state depending on the surface temperature, magnetic field strength, and composition. Different mathematical expressions can

be derived for radiation transport across such atmospheres to describe the effective beaming.

The Hopf beaming function:

$$I(\theta_m, \phi_m, \theta') = I_0(\theta_m, \phi_m)(\sum_{a=1}^{3} \frac{L_a}{1 + k_a cos(\theta')} - cos(\theta') + Q)$$

(Chandrasekhar 1950, eq. [III.50])[1], where L_a, k_a, and Q are given in Chandrasekhar (1950; Table III.VII), describes the beaming of radiation in a scattering-dominated atmosphere heated from below. As shown by Zavlin, Pavlov, Trümper (1998)[34], this beaming function is suitable to describe weakly magnetic H-He atmosphere at energies $\geq$1 keV.

At higher energies close to the electron cyclotron energy, the beaming functions do not decrease monotonically with θ'. For field strength of $\sim 10^{14} - 10^{15} G$ the cyclotron energy is $\sim$ 1-10 MeV which is much larger than the $\sim$ 1 keV energy of interest. It is reasonable to consider a beaming function that decreases monotonically with θ'. A general,sharper beaming function of the following form is used for strongly magnetized stars:

$$I(\theta_m, \phi_m, \theta') = I_0(\theta_m, \phi_m) cos^n(\theta')$$

The exponent of the cosine (n) defines the sharpness of the beaming.

Crucial effects on the shape and symmetry of the fully integrated pulse profile are observed due to the curvature of the photon trajectory due to relativistic effects combined with the θ' dependence introduced by the beaming function.

2.4 Flux Integration: Generating Pulse Profiles

The relativistic factor, surface intensity distribution, and the beaming function characterize all the physical parameters on the neutron star that affect the observed thermal emission. The final expression of flux emitted by a surface element dS on the stellar surface is given

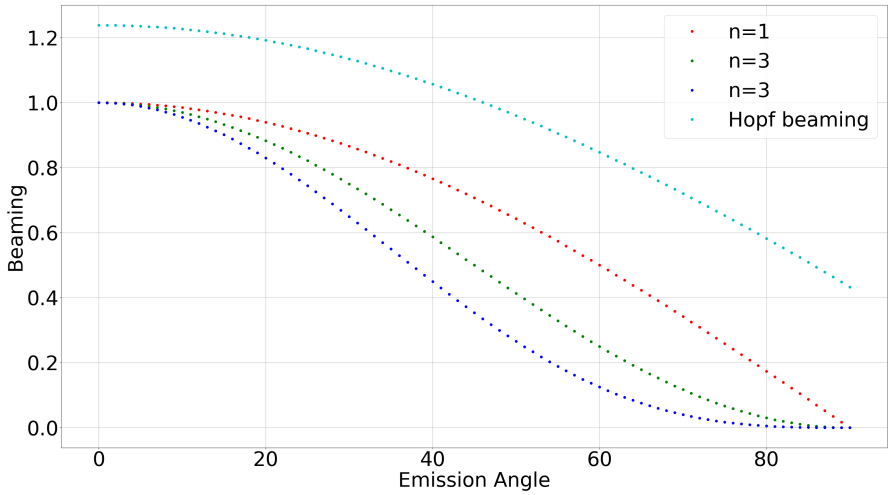

Figure 2.5: Radial dependence of the beaming functions. The strength of the cosine beaming function is described by the exponent 'n'. Hopf beaming function describes a scattering-dominated H-He atmosphere.

by:

$$dF = \left(1 - \frac{r_s}{R}\right)^2 I_0(\theta, \phi) B(\theta') \frac{dS}{D}$$

where D is the distance between NS and observer, dS is the surface element, $I_0(\theta_m, \phi_m)$ is the intensity distribution in magnetic coordinates(θ_m, ϕ_m), and $B(\theta')$ is the beaming function.

The next primary factors that affect the shape of the pulse profile are the viewing geometry and the physical geometry of the neutron star. The three important axes: the rotation axis, the magnetic axis, and the line of sight(los) axis, define three coordinate frames on the stellar surface. In the subsequent sections, the coordinates for the rotational frame are (θ_r, ϕ_r), for the magnetic frame are (θ_m, ϕ_m), and for the line of sight frame are $(\theta_{los}, \phi_{los})$.
After specifying the angles between the rotation and magnetic axes (α) and the line of sight and rotation axes (β), rotation matrices can be used to transform one coordinate frame into another.

$$\mathrm{R}_x(\theta) = \begin{pmatrix} 1 & 0 & 0 \\ 0 & \cos(\theta) & \text{-}\sin(\theta) \\ 0 & \sin(\theta) & \cos(\theta) \end{pmatrix} ; R_y(\theta) = \begin{pmatrix} \cos(\theta) & 0 & \sin(\theta) \\ 0 & 1 & 0 \\ \text{-}\sin(\theta) & 0 & \cos(\theta) \end{pmatrix}$$

$$R_z(\theta) = \begin{pmatrix} \cos(\theta) & \text{-}\sin(\theta) & 0 \\ \sin(\theta) & \cos(\theta) & 0 \\ 0 & 0 & 1 \end{pmatrix}$$

The stellar surface is divided into a grid with a specific angular width in the longitudinal and the latitudinal directions in the rotation coordinate frame. The grid provides a matrix of points defined by their coordinates (θ_r, ϕ_r). The rotation frame can be rotated by angle α to obtain a matrix of the grid points in the magnetic frame (θ_m, ϕ_m). Using the intensity distribution $(I_0(\theta_m, \phi_m))$, we get a matrix of the flux contribution from each grid point.

The bending of photon trajectory due to general relativity makes more than half of the stellar surface visible. The angle of emission at the surface can not exceed $\pi/2$. Using the Beloborodov approximation (see section 2.1), the angle of emission at all the grid points can be back-calculated. Any points with an angle of emission exceeding the limit lie in the invisible region. To obtain the bolometric flux, the intensity of emission combined with the beaming function for all the visible points must be integrated using the formula mentioned above.

The final step to generate the pulse profile is to compute the bolometric flux as described above for all rotational phase angles. The line of sight frame remains stationary, however, the rotation frame turns continuously with respect to the line of sight frame as the neutron star rotates. The rotation frame must be continuously transformed by the phase angle along the rotation axes to describe the observed surface of a rotating star. Repeating the exact same procedure for bolometric flux calculation gives the observed flux value for all phase angles.

Thus, by performing continuous coordinate transforms between the three coordinate frames described by the rotation, the magnetic, and the line of sight axes; and computing the bolometric flux after calculating the visible region of the stellar surface, intensity contribution from each grid point, and the beaming of radiation; the pulse profile of thermal emission can be generated for any viewing geometry, surface thermal map, gravitational strength, and beaming function.

Chapter 3

Analysis Method and Observations

In this chapter the method of performing a population study of parameters or combination of parameters that identify certain asymmetries in the stellar surface thermal map is described. First, an example study is presented which was used to check the general relativistic ray tracing code developed in this work. Next, the data of the observed isolated neutron stars are described and the asymmetries observed in their pulse profiles are used to introduce further parameters to study the 'distorted-dipole' thermal structure.

3.1 Population Study

Observations of asymmetric and multi-peaked pulse profiles from isolated neutron stars have motivated several studies to try to recreate profiles from individual sources considering specific magnetic field structures. For example; de Lima, Coelho, et al. recreated the pulse profile of SGR J1745-2900 by considering a multipolar field with 2-3 poles [11], and Bogdanov, Rybicki, Grindlay (2007) recreated the pulse profile of the millisecond pulsar PSRJ0437-4715 by considering an off-center magnetic axis [5].

The thermal emission from neutron stars is affected by a variety of factors that can alter the shape of the profile and different surface thermal maps can yield similar pulse profiles depending on the viewing geometry. A population study of parameters that target specific asymmetries in the surface thermal map, and hence, the magnetic field structure, such as

the one done by Hu, Ng, Ho (2019) [18], establishes the hypothesis more concretely.
In their study, Hu, Ng, and Ho [18], looked at the pulse profiles of 18 magnetars and tried to explain their asymmetric nature by considering stronger emission from one hemisphere of the magnetars. Their simulation generated pulse profiles with $\frac{R_s}{R} = \frac{1}{3}$, Hopf beaming function, and the following intensity distribution:

$$I_0(\theta_m, \phi_m) = I_0 \frac{\cos^2 \theta_m}{(3\cos^2 \theta_m + 1)^{0.8}}$$

if the point is in the dimmer hemisphere, and

$$I_0(\theta_m, \phi_m) = r I_0 \frac{cos^2 \theta_m}{(3cos^2 \theta_m + 1)^{0.8}}$$

if the point is in the brighter hemisphere. 'r' is the intensity ratio. The RMS pulse fraction and the harmonic strength of the second Fourier component of the pulse profile are directly affected by the intensity ratio (r). Comparing the distribution of these two parameters for the simulated pulse profiles and the observed profiles gives an idea about the anisotropy in the surface thermal map of magnetars.

After taking the Fourier transform of a pulse profile, the Fourier components can be described as:

$$a_k = \frac{1}{N} \sum_{i=1}^{N} x_i cos(2\pi k \phi_i)$$

$$b_k = \frac{1}{N} \sum_{i=1}^{N} x_i sin(2\pi k \phi_i)$$

Components with $k \geq 6$ are ignored as they have negligible power. The harmonic strength of each component is calculated as:

$$A_k = \frac{\sqrt{a_k^2 + b_k^2}}{\sum_{j=1}^{5} \sqrt{a_j^2 + b_j^2}}$$

A pulse profile can be broken down into two components that correspond to the flux contribution from the two poles. If $A_k = 0$ for all $k > 1$, then the inverse Fourier transformed profile would be single-peaked sinusoidal. The second Fourier component adds another si-

nusoidal component that makes the profile double-peaked. Thus, single-peaked profiles have a lower value of A2 and double-peaked profiles have a higher value. In a qualitative sense, A2 describes the tendency of a profile towards being single-peaked or double-peaked. The distribution of A2 values for a population of profiles acts as a gauge of the number of double and single-peaked profiles. An intensity ratio greater than one enhances the contribution from one hemisphere and reduces the A2 value.

The RMS pulse fraction is calculated using the following formula:

$$PF = \frac{1}{a_0}\sqrt{2\sum_{k=1}^{5}[(a_k^2 + b_k^2) - (\sigma_{a_k}^2 + \sigma_{b_k}^2)]}$$

where,

$$\sigma_{a_k}^2 = \frac{1}{N^2}\sum_{i=1}^{N}\sigma_i^2 cos(2\pi k\phi_i)$$

$$\sigma_{b_k}^2 = \frac{1}{N^2}\sum_{i=1}^{N}\sigma_i^2 sin(2\pi k\phi_i)$$

are the Fourier power generated by the noise and σ_i is the uncertainty in x_i.
The pulse fraction gives a measure of the strength of the pulsation in the profile. It is directly dependent on the total flux variation observed in a rotation period which in turn depends on the surface thermal map. An intensity ratio greater than 1 increases the flux contribution from one hemisphere and results in a large PF for certain viewing geometries. Each thermal map has a maximum value of PF that can be observed. Comparing the range of PF distribution spanned by simulations with random viewing geometries with the observed data provides an idea of the anisotropies present in the thermal map.

The procedure to generate pulse profiles described above was used to create a population of profiles with randomized viewing geometry and intensity ratio $r = 1, 3, 9$. In addition, a population with random values of r uniformly distributed between 1 and 6 was created. The distributions of A2 and RMS pulse fraction created match the results obtained by Hu, et al.

The distributions of A2 and RMS PF follow the trends as explained above. The intensity ratio of one shows a flat A2 distribution and as the ratio is increased, the range spanned truncates. Oppositely, the range spanned by the RMS pulse fraction increases as the in-

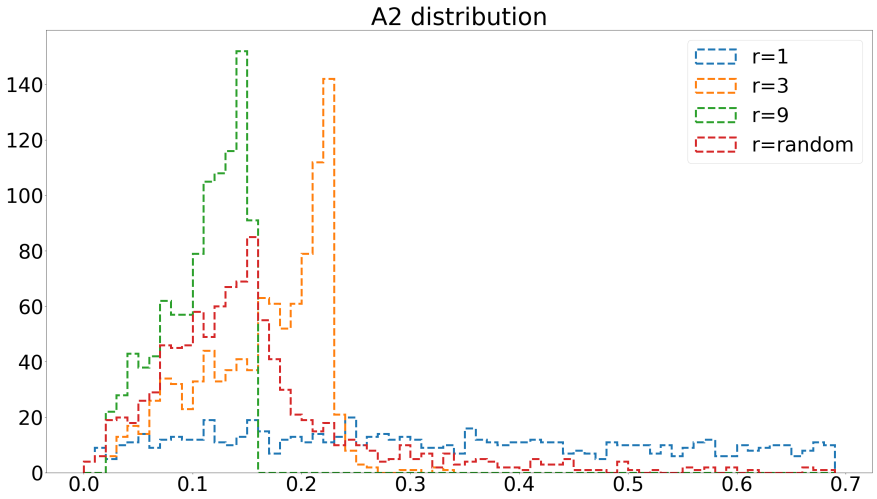

Figure 3.1: Distribution of A2 for different intensity ratios of the hot spots. Increasing the intensity ratio concentrates the value of A2 to a smaller range as the brighter hot spot dominates the emission and tends the profile to a more single-peak shape.

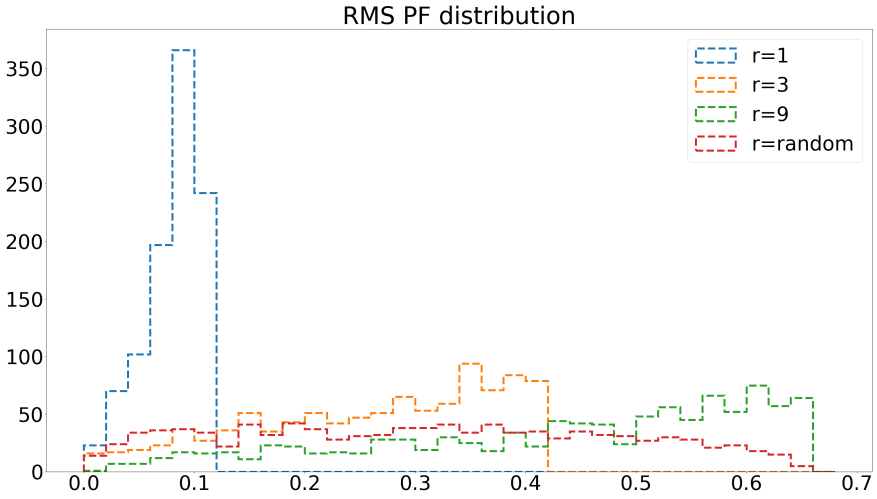

Figure 3.2: Distribution of the RMS pulse fraction for different intensity ratios of the hot spots. Increasing the ratio broadens the range of the pulse fraction. Depending on the geometry, an asymmetric temperature map can result in a low or high pulse fraction but a symmetric map will always give a small value.

tensity ratio is increased. Hu, et al. compared these results with the distribution of the 18 magnetars they considered and showed that the distribution corresponding to the random

intensity ratio (r randomly selected from a uniform distribution between 1 to 9) matches the observed data best. This implies that the intensity ratio varies greatly from one source to another and certain asymmetries in the pulse profiles can be explained only if an asymmetric surface thermal map is considered.

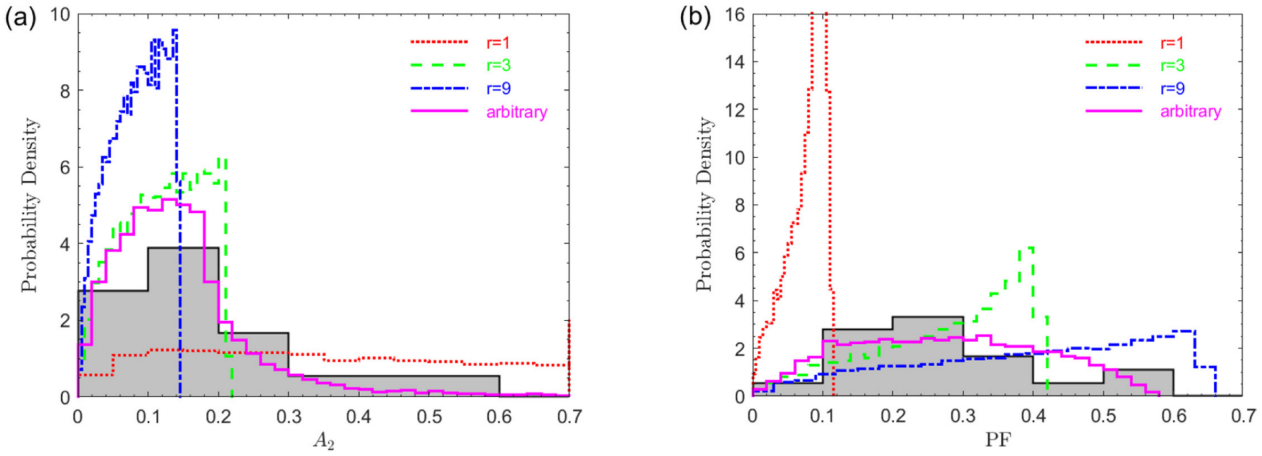

Figure 3.3: Distribution of the RMS pulse fraction and A2 calculated by Hu, et al. and the comparison with observed data. The distributions for a random intensity ratio taken from a uniform distribution between 1 to 9 fit the data best. The figure is taken from [18].

A2 and RMS pulse fraction are two parameters that are directly calculable from the pulse profile. They are directly affected by the intensity ratio chosen to describe the surface thermal map. Comparison of the distribution of these parameters for a simulated population for randomized viewing geometries with the observed data helps make concrete statements regarding the presence of such anisotropies in the thermal map of actual sources. The asymmetric pulse profiles observed from isolated neutron stars can not be solely explained by introducing an intensity ratio in the thermal distribution. The simulation program considers cases with a secondary pole deviated from the antipodal position and an intensity ratio. To analyze the simulations with more complex surface thermal maps, parameters other than A2 and RMS PF that are directly affected by the deviation of the secondary pole must be considered.

3.2 Observed Data

The data set of observations provided to me and used in my analysis consists of pulsed profiles from thirty-four isolated neutron stars. All the observations were done with XMM-Newton using the European Photon Imaging Cameras (EPIC). The $EPIC - MOS1/2$ cameras (Turner et al. 2001)[30] were operated in full-window mode (time resolution 2.6 s) with medium and thin optical filter, while the EPIC-pn camera (Strüder et al. 2001)[27] was in small-window mode (time resolution 5.7 ms) with the thin filter. The data reduction was done using the $EPPROC$ and $EMPROC$ pipelines of version 18 of the Scientific Analysis Software (SAS). The barycentric corrections were done using the $JPLDE405$ ephemeris with the tool *barycen*. Source counts were selected in a circular region of radius $30''$, while the background was chosen far away from the pulsar and avoiding the region of tail-emission.

The observed sample consists of old and middle-aged rotation-powered pulsars (RPPs), XDINS, CCOs, and highly magnetized pulsars (HBPs). The best fit of the pulse profile of each source is categorized into three classes: single-peaked, double-peaked, and complex-structured. The corresponding parameters are calculated and listed in table 3.1. Five of the thirty-four sources show a double-peaked profile and only one shows a complex-structured profile. The rest are single-peaked.

The fits are obtained by subsequently adding Fourier components to get a smooth fit without over-fitting the data with poor statistics. As seen in Figures 3.4 and 3.5, asymmetries such as: unequal maxima and minima in double-peaked profiles, phase difference less than π between the peaks of double-peaked profiles, single-peaked profiles which are skewed to one side, and profiles with more than two peaks are evident. These asymmetries can be explained by the surface thermal map corresponding to the 'distorted-dipole' magnetic field structure. To quantify these asymmetries, further parameters other than A2 and RMS PF are introduced.

3.3 Further Parameters

Four new parameters are introduced in this work. The combinations of these parameters with each other and the two previous parameters (A2 and RMS pulse fraction) describe the

Source	Type	Profile	A2	RMS PF	Skew	MM ratio	mm ratio	Peak Separation
B0656	RPP middle	Double Peaked	0.15	0.07	N/A	1.23	1.0	2.65
B0823	RPP middle	Single Peaked	0.06	0.55	0.19	N/A	N/A	N/A
B0833	RPP middle	Complex Structured	N/A	N/A	N/A	N/A	N/A	N/A
B0893	RPP old	Single Peaked	0.09	0.18	0.09	N/A	N/A	N/A
B0950	RPP old	Single Peaked	0.25	0.19	-0.06	N/A	N/A	N/A
B1055	RPP middle	Single Peaked	0.18	0.37	-0.08	N/A	N/A	N/A
B1706	RPP middle	Single Peaked	0.21	0.08	-0.02	N/A	N/A	N/A
B1822	RPP middle	Single Peaked	0.14	0.23	-0.10	N/A	N/A	N/A
B1929	RPP old	Single Peaked	0.15	0.16	-0.07	N/A	N/A	N/A
J0007	RPP middle	Single Peaked	0.16	0.12	0.06	N/A	N/A	N/A
J0108	RPP old	Single Peaked	0.10	0.45	-0.16	N/A	N/A	N/A
J0357	RPP old	Single Peaked	0.14	0.16	0.04	N/A	N/A	N/A
J0420	XDINS	Single Peaked	0.14	0.11	-0.04	N/A	N/A	N/A
J0538	RPP middle	Single Peaked	0.22	0.13	-0.04	N/A	N/A	N/A
J0632	RPP middle	Single Peaked	0.02	0.13	0.04	N/A	N/A	N/A
J0633	RPP middle	Double Peaked	0.26	0.31	N/A	1.43	1.0	1.98
J0720	XDINS	Double Peaked	0.66	0.02	N/A	1.01	1.0	2.98
J0726	HBP	Double Peaked	0.75	0.21	N/A	1.00	1.0	3.31
J0806	XDINS	Single Peaked	0.17	0.03	0.01	N/A	N/A	N/A
J0821	CCO	Single Peaked	0.12	0.09	-0.03	N/A	N/A	N/A
J1119	HBP	Single Peaked	0.18	0.42	0.16	N/A	N/A	N/A
J1210	CCO	Single Peaked	0.06	0.06	-0.03	N/A	N/A	N/A
J1308	XDINS	Double Peaked	0.59	0.11	N/A	1.00	1.0	2.65
J1357	RPP middle	Single Peaked	0.16	0.18	0.06	N/A	N/A	N/A
J1412	RPP middle	Single Peaked	0.07	0.15	-0.09	N/A	N/A	N/A
J1740	RPP middle	Single Peaked	0.16	0.10	0.04	N/A	N/A	N/A
J1741	RPP middle	Single Peaked	0.17	0.26	-0.10	N/A	N/A	N/A
J1819	HBP	Single Peaked	0.12	0.24	-0.09	N/A	N/A	N/A
J1836	RPP middle	Single Peaked	0.14	0.34	-0.17	N/A	N/A	N/A
J1852	CCO	Single Peaked	0.07	0.35	-0.15	N/A	N/A	N/A
J1856	XDINS	Single Peaked	0.04	0.01	0.00	N/A	N/A	N/A
J1957	RPP middle	Single Peaked	0.07	0.13	0.06	N/A	N/A	N/A
J2021	RPP middle	Single Peaked	0.14	0.70	0.21	N/A	N/A	N/A
J2143	XDINS	Single Peaked	0.13	0.02	0.01	N/A	N/A	N/A

Table 3.1: Source type, pulse profile classification, and parameter values calculated for the observed data.

effects of the two asymmetries considered in the thermal map.

- **Skewness** is the measure of the tilt of a single-peaked pulse profile towards the left or the right. Deviating the secondary pole and a non-unity intensity ratio merges the flux contribution from the two poles and shows a peak at a phase angle different from when the primary pole crosses the plane of view. The tilt is calculated by considering the third central moment of a distribution that replicated the pulse profile. For a

distribution, the skewness is calculated as:

$$\mu_n = E[(X - E[x])^n] = \int_{-\infty}^{+\infty} (x - \mu)^n f(x) dx$$

μ_n is the nth moment of a distribution with real, random variable X. E is the expectation operator, f(x) is the probability density function, and μ is the mean. μ_3 is the skewness value. A distribution skewed to the left has a negative skewness value and a distribution skewed to the right has a positive skewness value. A perfectly symmetric distribution has zero skewness.

- **MM and mm** are defined as the ratios of the two maxima and the of the two minima, respectively, for double-peaked profiles. The net flux variation is quantified by the RMS pulse fraction, however, deviating the second pole from the antipodal position concentrates the bright region in a smaller area and merges the flux contribution from the two poles. Thus, the ratio of the maxima (i.e. of the two peaks) gives a lower value for higher deviation and the ratio of the two minima gives a higher value. A combined analysis of the two ratios can give a measure of the deviation of the secondary pole.

- **Peak separation** is the phase difference between the two peaks in a double-peaked pulse profile. The peaks in a double-peaked profile are observed when the poles cross the plane of sight as the pulsar rotates. Deviating the second pole from the antipodal position can shift its phase compared to the antipodal case, thus the peak separation can be smaller than π. The angular separation between the peaks is a direct measure of the deviation of the secondary pole.

The pulse profiles can be simulated for any viewing geometry after fixing the physical properties of the neutron star. The GR factor, surface thermal distribution, and beaming of radiation in the atmosphere affect the shape of the final pulse profile. A population study considering specific parameters that are directly affected by the asymmetries in the thermal map gives concrete results about the presence of such asymmetries in actual sources. Using the RMS pulse fraction and A2, the results of [18] about anisotropic thermal maps on magnetars were recreated. The asymmetric pulse profiles can be recreated by considering a secondary pole deviated from the antipodal position with an intensity ratio. To do a population study for this case, new parameters that are directly affected by the deviation angle of the second pole are introduced.

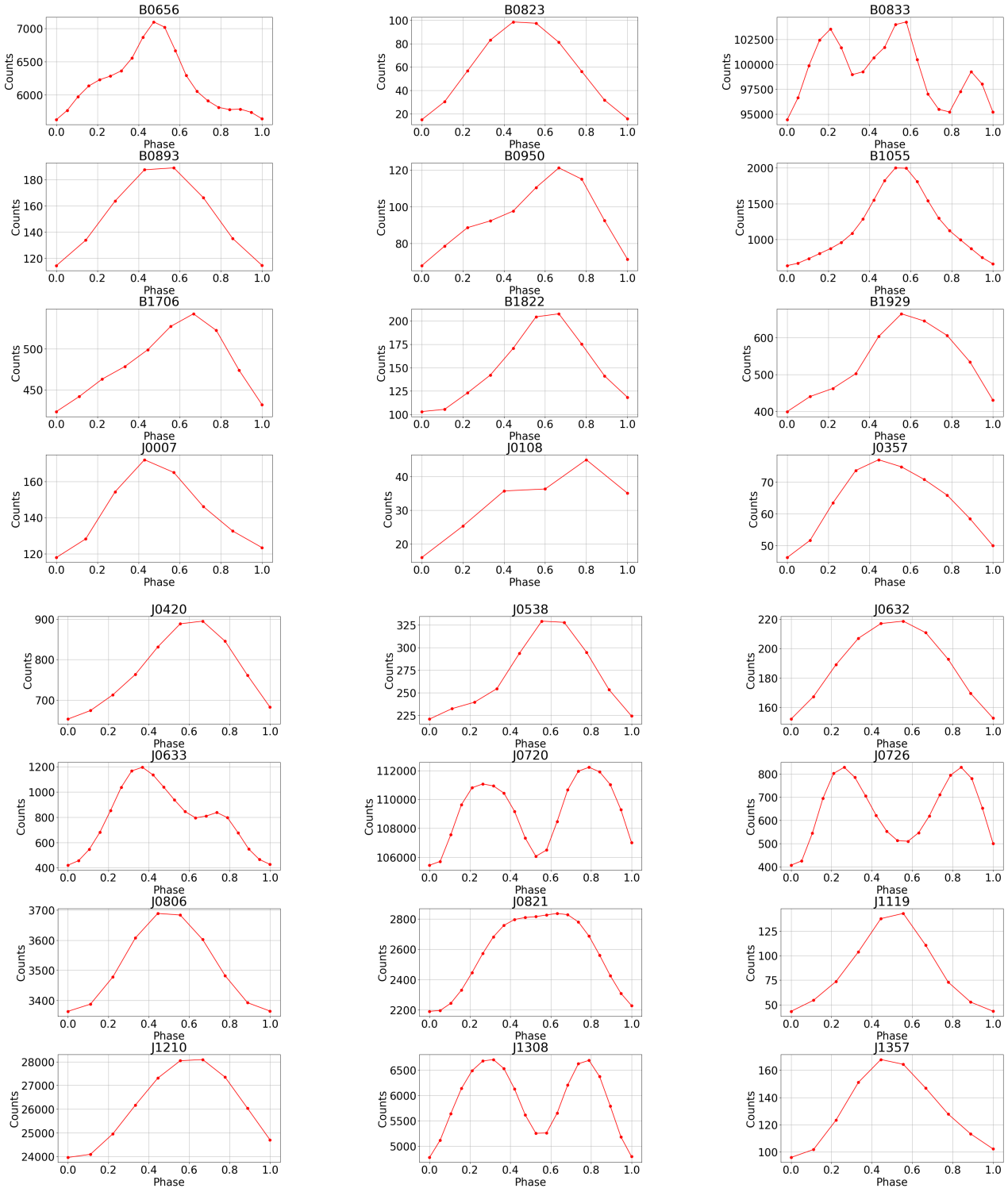

Figure 3.4: Pulse profiles (in counts per bin) in the soft x-ray energy range for the observed sources. The pulse profiles are background subtracted.

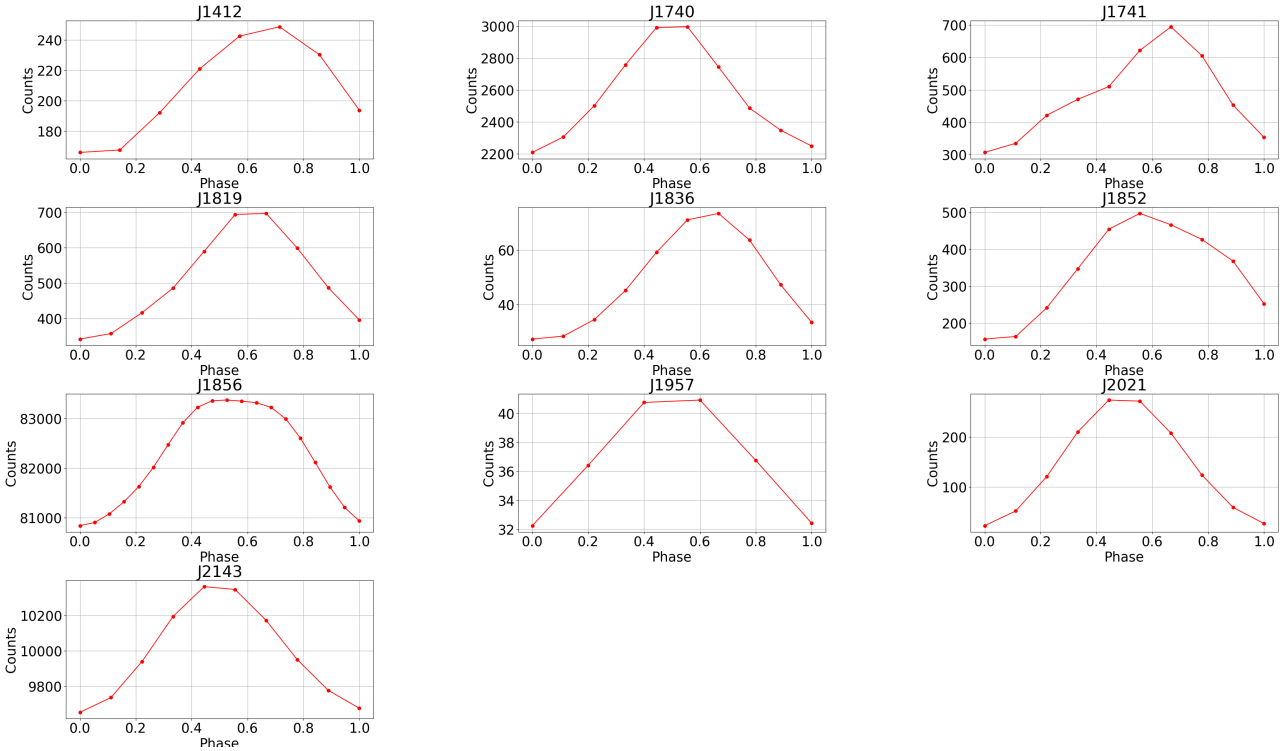

Figure 3.5: Pulse profiles (in counts per bin) in the soft x-ray energy range for the observed sources. The pulse profiles are background subtracted.

Chapter 4

Results

The asymmetries in the observed profiles can be explained by the two primary deviations from the standard model of neutron stars under consideration. Using the pulse profile generating program, one thousand profiles for different deviation angles of the secondary pole from the antipodal spot and different intensity ratios of the poles are created to obtain the distributions of the parameters resulting from these specific asymmetries.

Cumulative parameter distributions for specific intensity ratios and secondary pole deviation help to identify the individual effects of these asymmetries on the parameter distributions.

4.1 RMS Pulse Fraction Distributions

The RMS pulse fraction gauges the strength of the pulsation of the profiles. It is directly affected by the thermal map and the variation in the total flux over a rotation period. Higher intensity ratio and greater deviation of the secondary pole increases the flux variation over a period and results in a larger pulse fraction.

As is evident in the figure 4.1, increasing the deviation angle for a fixed intensity ratio broadens the range spanned by the pulse fraction values. Increasing the intensity ratio allows the contribution from the primary pole to dominate and produce greater flux variations over a rotation period which gives higher pulse fraction values. At high intensity ratios, the effect

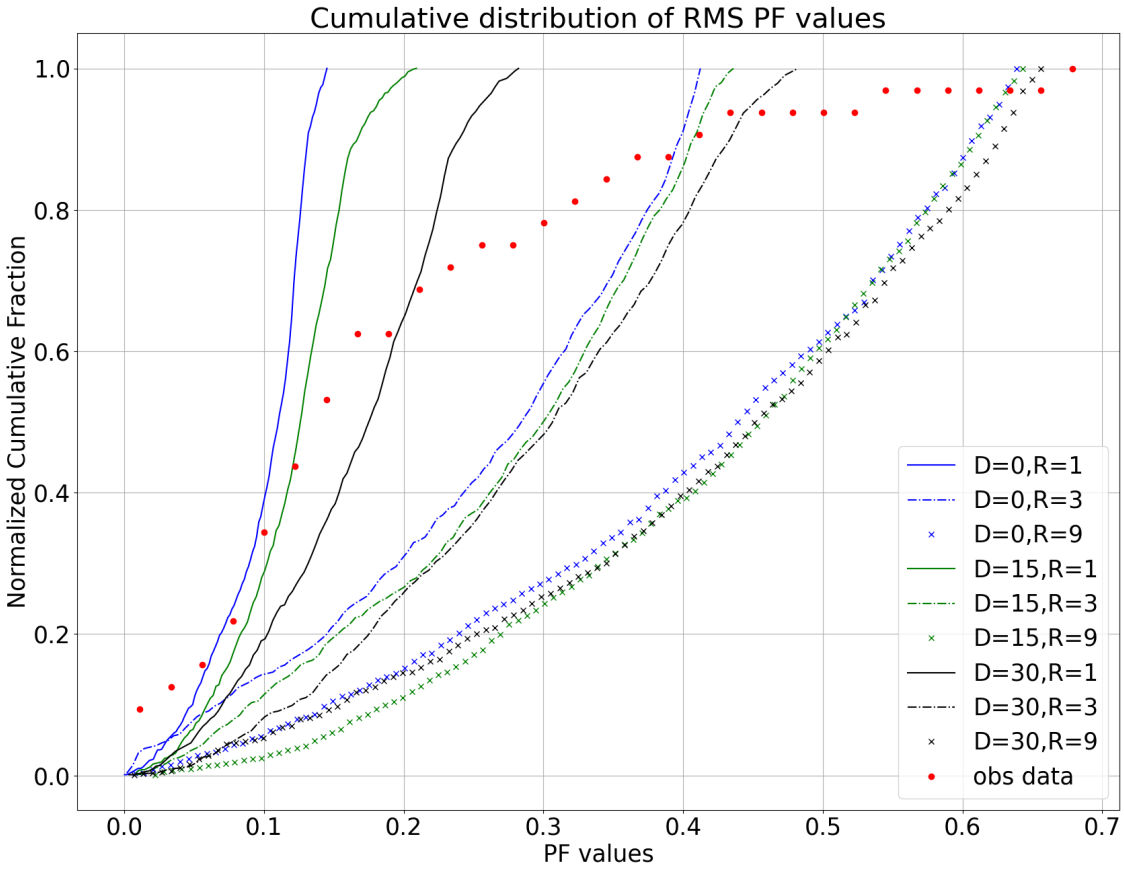

Figure 4.1: Distribution of RMS PF values for different deviation angles of the secondary pole and intensity ratios. 'D' is the deviation angle in degrees and 'R' is the intensity ratio. The distributions are for the populations of the profiles created with low beaming strength (n=1).

of deviation of the secondary pole is diminished. In the case of R=9, the primary pole always dominates and the effect due to deviation of the secondary pole is difficult to identify.

The cases with intensity ratio $R = 1$ are immediately ruled out upon comparison with the distribution of the observed data. Increasing the intensity ratio never gives a distribution with a shape that matches that of the observed data. For $R = 9$, more than sixty percent of the profiles show a pulse fraction value over 0.4 whereas more than sixty percent of the observed profiles show a value less than 0.2.

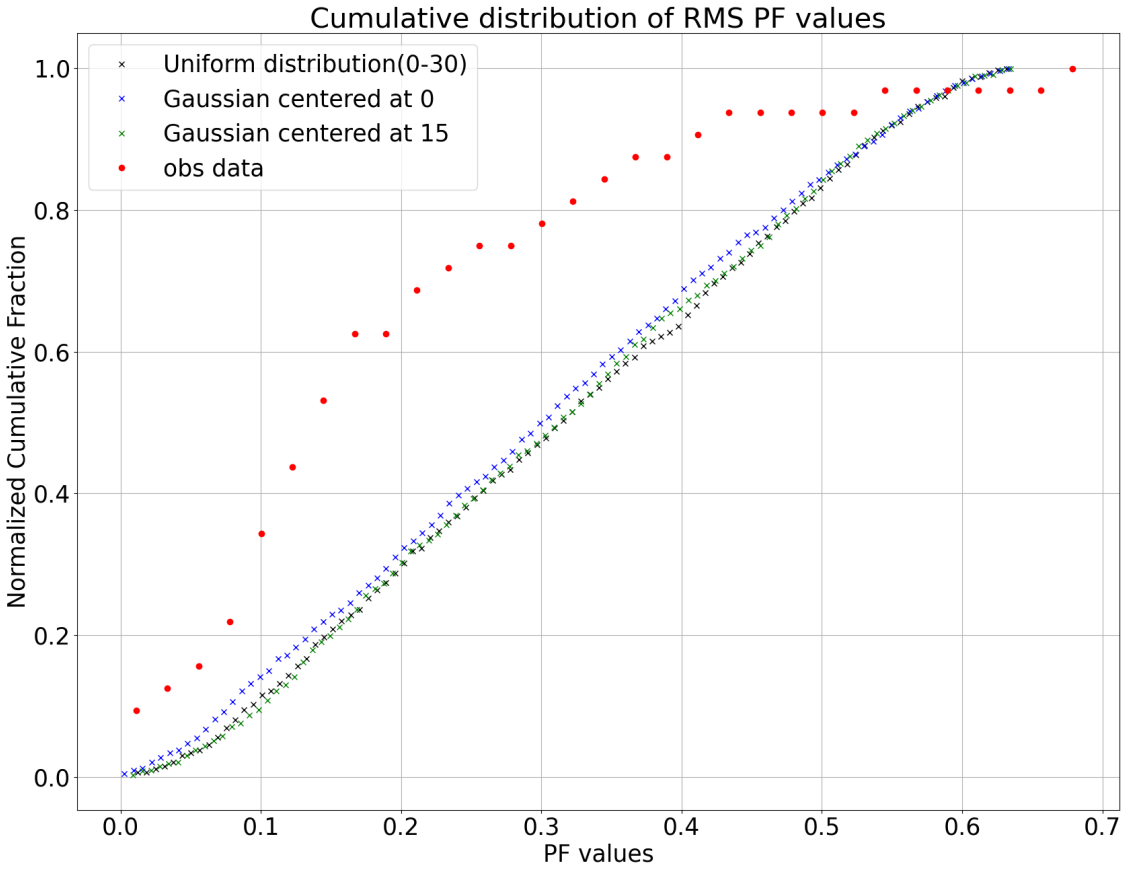

Figure 4.2: Distributions of RMS PF values obtained from a population of profiles generated for a randomly selected intensity ratio (R) from a uniform distribution between 1 and 9, and a random deviation angle (D) selected from a uniform distribution between 0 and 30 degrees, a Gaussian distribution centered at 15 degrees with a variance of 10 degrees, and a Gaussian distribution centered at 0 degrees with a variance of 15 degrees.

In the case of Magnetars studied above (see chapter 3), a good fit to the observed RMS PF distribution was obtained by a population of neutron stars with random distribution of intensity ratios. As shown in figure 4.1, no distribution for any intensity ratio fits the observed data well. However, the distributions for populations of profiles generated for a randomly selected intensity ratio (R) from a uniform distribution between 1 and 9, and a random deviation angle (D) selected from a uniform distribution between 0 and 30 degrees, a Gaussian distribution centered at 15 degrees with a variance of 10 degrees, and a Gaus-

sian distribution centered at 0 degrees with a variance of 15 degrees give a closer fit to the observed data (see figure 4.2) . The difference in the distributions for each population is negligible.

This implies that the intensity ratio and the deviation of the secondary pole from the antipodal point varies greatly from source to source. It is possible to obtain a better fit to the data only if both asymmetries in the surface thermal map are considered. It must also be considered that the observed data are affected by some biases which, if taken into account, could either reduce or increase the discrepancies with the simulated populations. For example, it is difficult to detect pulsations from faint sources when the pulse fraction is low. This means that thermally emitting neutron stars with small pulse fractions are underrepresented in our sample. Accounting for this bias would concentrate the distribution towards smaller pulse fraction values and further increases the discrepancy from the randomized distribution.

4.2 A2 Distributions

A2 is the strength of the second harmonic Fourier component of the pulse profiles. It is a measure of the tendency of the profile towards being double peaked. Single peaked profiles have a smaller value of A2 and double peaked profiles have a larger value. The distribution of A2 acts as a gauge of the fraction of single and double peaked profiles present in a population with specified intensity ratio and secondary pole deviation angle.

The completely symmetric case, i.e., the antipodal case with R=1, should show an equal number of single and double-peaked profiles irrespective of the beaning function and GR factor for randomly selected viewing geometries. This observation was also evident during the recreation of the A2 distribution as done by Hu, et al. for Magnetars. A2 shows a flat uniform distribution; in the cumulative plot, this is evident as an almost straight line. Introducing further asymmetries in the surface thermal map concentrates the distribution towards lower values. Increasing the deviation of the secondary pole from the antipodal point concentrates the brighter areas in a smaller region which makes the observation of single peaked profiles more likely for randomly selected viewing geometries. Increasing the intensity ratio allows the brighter pole to dominate over the secondary pole and makes the

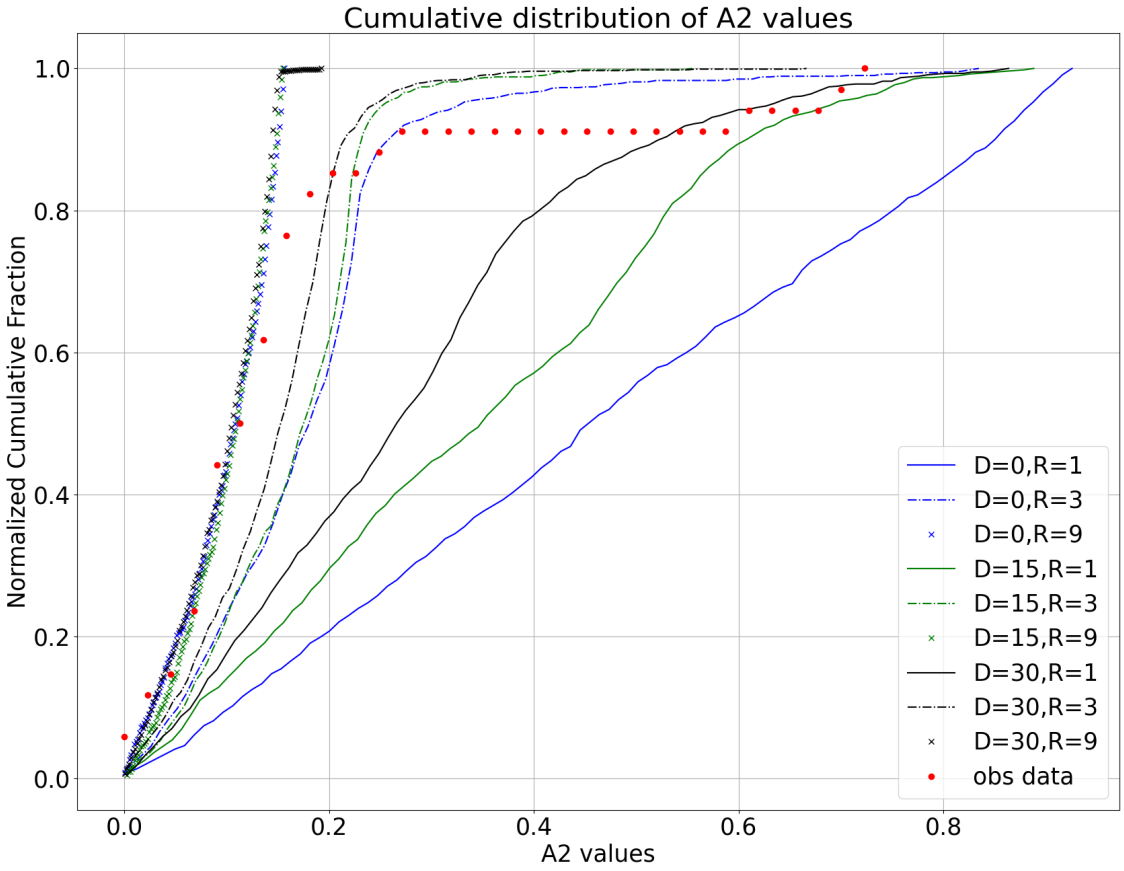

Figure 4.3: Distribution of A2 values for different deviation angles of the secondary pole and intensity ratios. 'D' is the deviation angle in degrees and 'R' is the intensity ratio. The distributions are for the populations of the profiles created with low beaming strength (n=1).

observation of single-peaked profiles more probable as well as gives the double-peaked profiles a 'single peaked nature' as the contribution from the secondary pole is less compared to the primary pole.

From the plot we see that for the same intensity ratios, increasing the deviation angle of the secondary pole shifts the plot towards smaller A2 values. Increasing the intensity ratio concentrates the A2 values in a smaller range. For the extremely high-intensity ratio (R=9) the contribution from the primary pole dominates over the secondary pole and the deviation angle has a negligible effect.

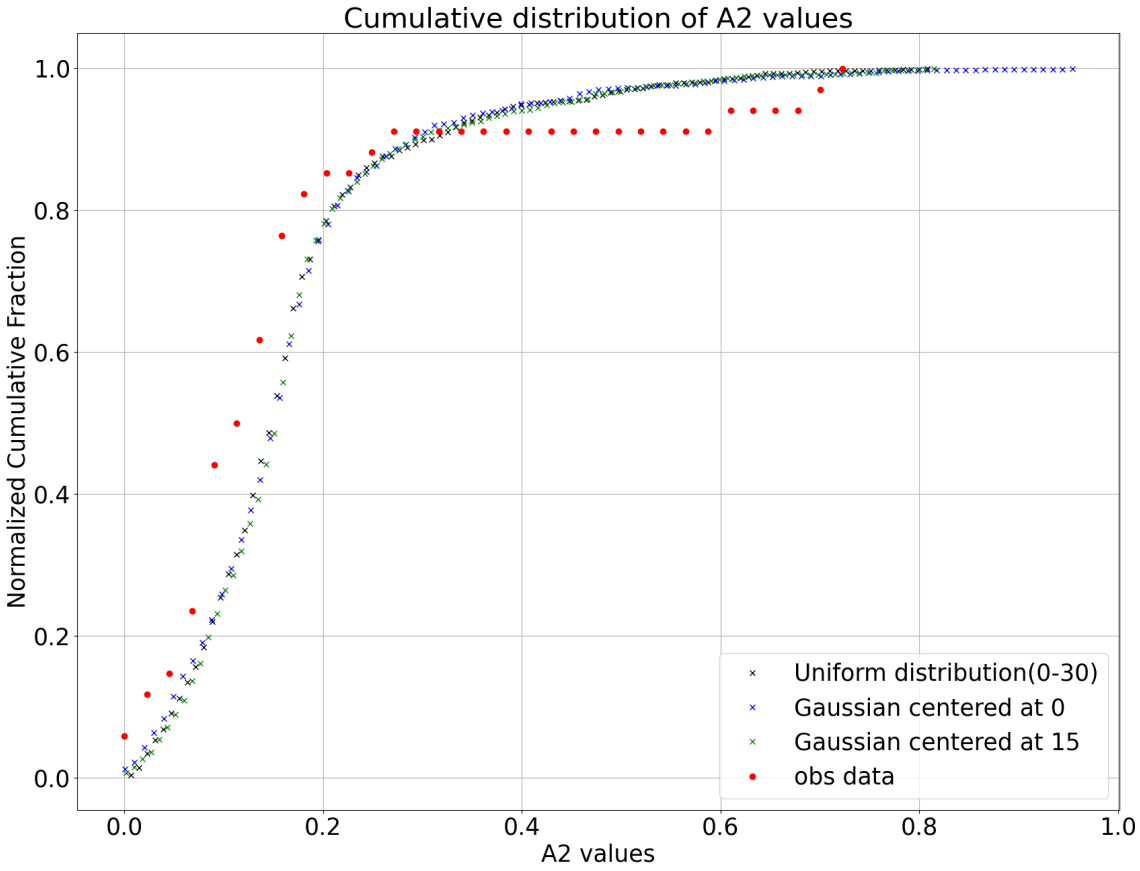

Figure 4.4: Distribution of A2 values obtained from a population of profiles generated for a randomly selected intensity ratio (R) from a uniform distribution between 1 and 9, and a random deviation angle (D) selected from a uniform distribution between 0 and 30 degrees, a Gaussian distribution centered at 15 degrees with a variance of 10 degrees, and a Gaussian distribution centered at 0 degrees with a variance of 15 degrees.

The distribution of the observed data spans a narrower range compared to the standard dipolar model and more than ninety percent of the profiles have an A2 value less than 0.3. The difficulty to accurately fit profiles with poor statistics results in fits that may be biased towards being single peaked, but such a large concentration at small A2 values is not expected.

The distribution of the observed data is fit well with populations of profiles generated for a

randomly selected intensity ratio (R) from a uniform distribution between 1 and 9, and a random deviation angle (D) selected from a uniform distribution between 0 and 30 degrees, a Gaussian distribution centered at 15 degrees with a variance of 10 degrees, and a Gaussian distribution centered at 0 degrees with a variance of 15 degrees.(see figure 4.4). The difference in the distributions for each population is negligible. This implies that the surface thermal map varies greatly from source to source and it is not symmetric as expected in the standard, dipolar case.

4.3 A2 versus PF

The intensity ratio determines the relative contribution to the total flux from each pole and the deviation angle determines the region in which the bright regions are concentrated. Together, they have an opposing effect on the range spanned by the distributions of A2 and RMS PF. Figure 4.5 shows RMS PF versus A2 of the simulated profiles compared with the observed data for weak beaming ($n = 1$). For lower intensity ratios, the RMS PF is systematically low and A2 spans a broad range. As the ratio is increased, the range of A2 truncates and the range of RMS PF broadens. As the deviation angle of the secondary spot from the antipodal point is increased, the range spanned by A2 at low intensity ratios increases because the flux contribution from the two poles merges.
Most of the observed sources lie within the region covered by the simulated profiles for different intensity ratios at all deviation angles. Increasing the beaming strength will result in cases with high A2 and high PF, however, none of the observed sources show these properties.

4.4 Skewness Distributions

Non-dipolar surface temperature distributions can result in lopsided single peaked profiles where the pulses are tilted to the left or the right. This asymmetry can be quantified by the skewness parameter defined in the previous chapter.
For the cases with antipodal secondary hotspots, single-peaked profiles should always be symmetric irrespective of the intensity ratio or the viewing geometry as the flux contribution

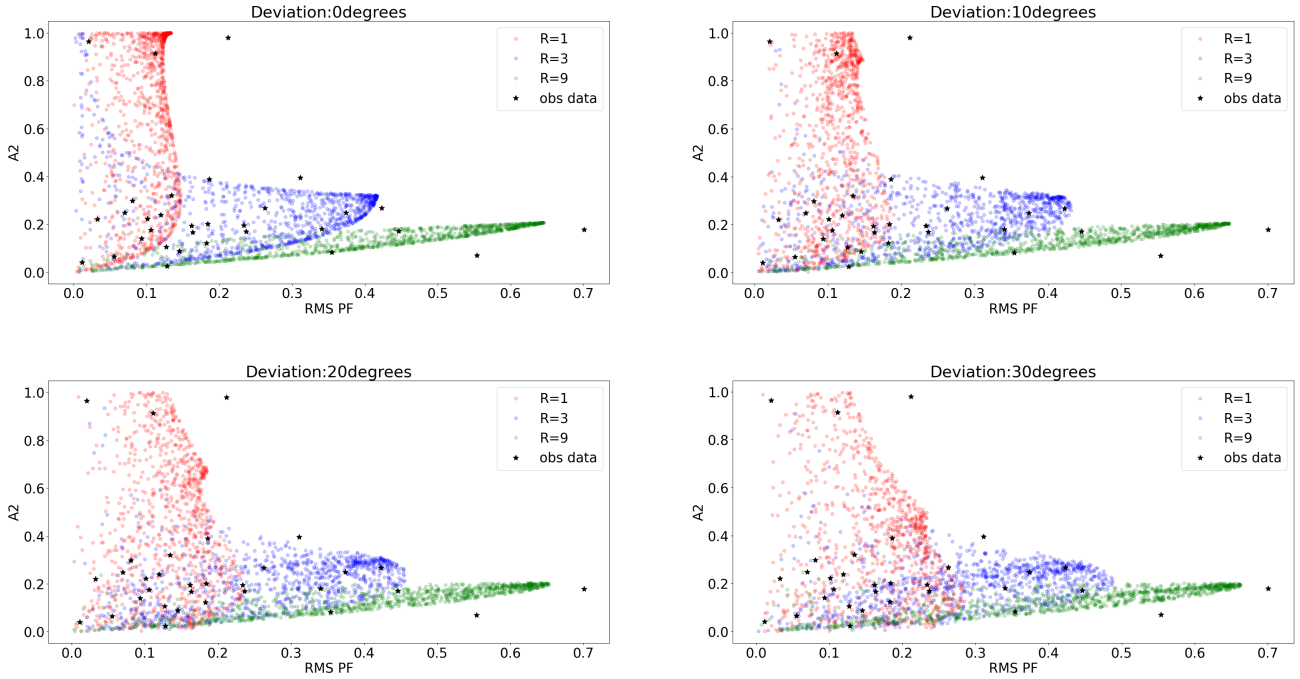

Figure 4.5: A2 versus RMS PF for the observed and simulated pulse profiles. The red, blue, and green points represent the simulated profiles for different intensity ratios (R). The black points represent the observed profiles. The plots are made assuming weak beaming ($n = 1$) for different deviation angles of the secondary pole.

is symmetric across the peak phase. Deviating the secondary hotspot and considering higher intensity ratios merges the flux contribution from the two poles and results in a lopsided profile with the peak at a phase value different from when the primary hotspot crosses the plane of view.

The figure 4.6 shows the distribution of skewness values calculated for the simulations and for the observations. Equally distributed positive and negative skewness values are observed as the viewing geometry and deviation of the secondary hotspot are randomized. The symmetric, dipolar case shows a very narrow range of skewness values, close to zero. Ideally, the skewness values for this case should always be zero; however, non-zero values (very close to zero) are obtained due to computational limits while creating a distribution of random parameters to recreate the profile. Introducing deviation and higher intensity ratios broadens the range of skewness observed. At a very high-intensity ratios, the contribution from the primary hotspot dominates and renders the merging of fluxes from the two hemispheres

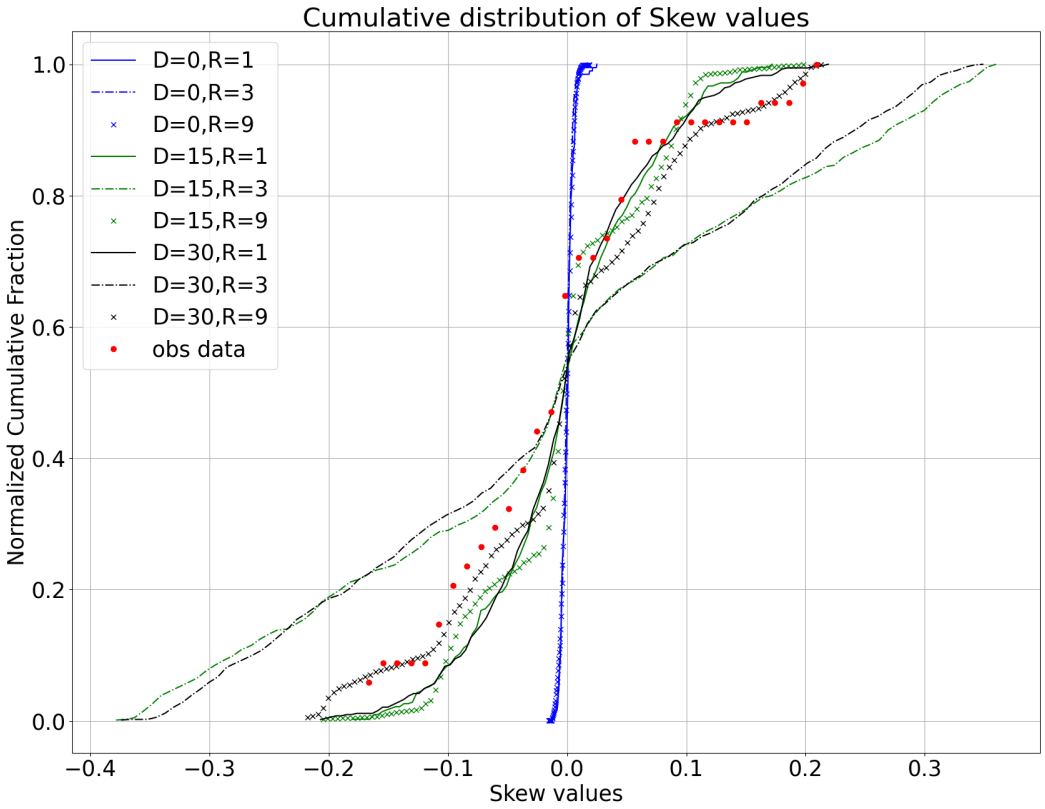

Figure 4.6: Distribution of Skewness values of single-peaked profiles of a population for different deviation angles of the secondary pole and intensity ratios. 'D' is the deviation angle in degrees and 'R' is the intensity ratio. The distributions are for the populations of the profiles created with low beaming strength (n=1).

insignificant. Thus, the range truncates at high-intensity ratios.

The symmetric, antipodal case is immediately rejected upon comparison with the distribution of the observed single-peaked profiles as it can not yield large skewness values. Increasing the deviation of the secondary hotspot and the intensity ratio have an opposing effect on the range of skewness values spanned by the distribution. However, distributions of A2 values obtained from a population of profiles generated for a randomly selected intensity ratio (R) from a uniform distribution between 1 and 9, and a random deviation angle (D) selected from a uniform distribution between 0 and 30 degrees, a Gaussian distribution centered at 15 degrees with a variance of 10 degrees, and a Gaussian distribution centered

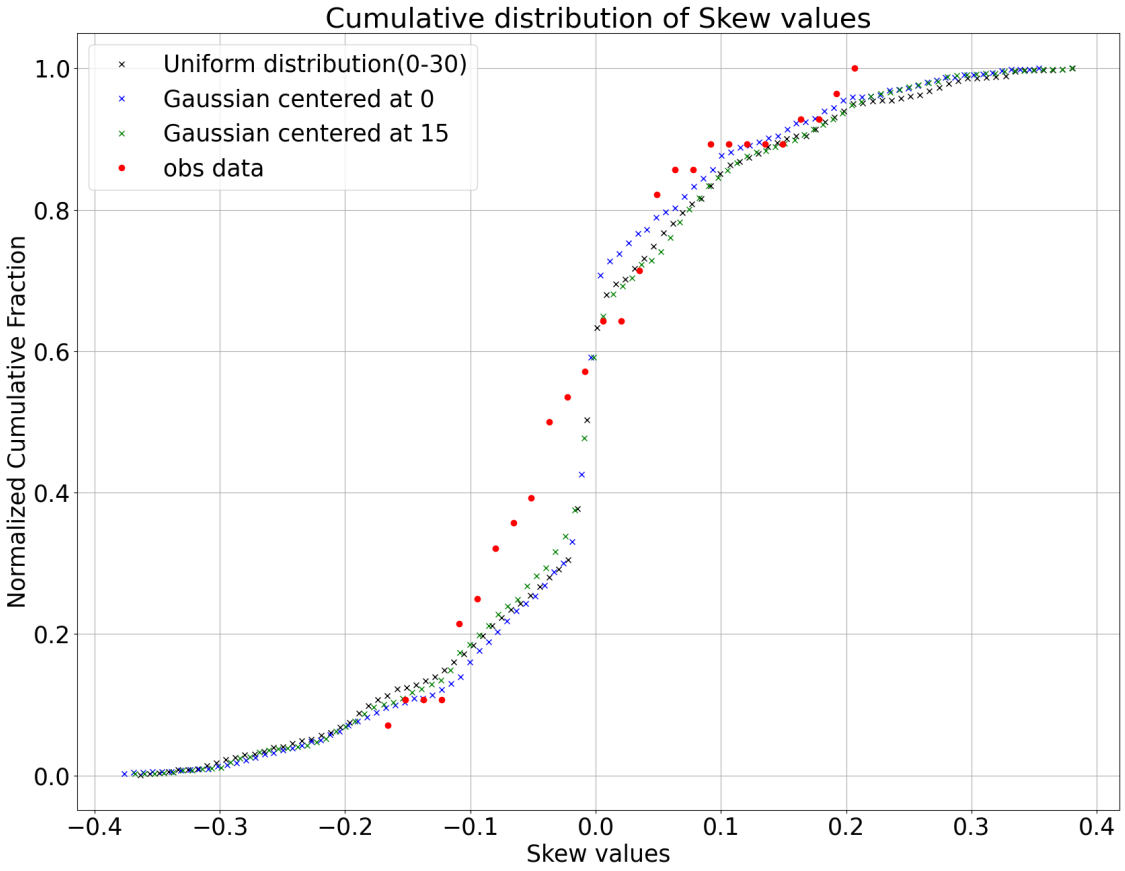

Figure 4.7: Distribution of Skewness values obtained for the single-peaked profiles from a population of profiles generated for a randomly selected intensity ratio (R) from a uniform distribution between 1 and 9, and a random deviation angle (D) selected from a uniform distribution between 0 and 30 degrees, a Gaussian distribution centered at 15 degrees with a variance of 10 degrees, and a Gaussian distribution centered at 0 degrees with a variance of 15 degrees.

at 0 degrees with a variance of 15 degrees give a closer fit to the observed data (see 4.7). The difference in the distributions for each population is negligible.

This implies that the intensity ratio and the deviation of the secondary pole from the antipodal point varies greatly from source to source. It is possible to obtain a better fit to the data only if both asymmetries in the surface thermal map are considered.

Deviation	1	3	9	Rand
0	80.3	50.6	0.0	41.5
5	69.5	33.2	0.0	29.2
10	60.7	13.6	0.0	24.4
15	57.7	8.9	0.0	16.8
20	51.7	5.9	0.0	16.7
25	48.4	6.2	0.0	12.7
30	47.0	4.2	0.0	9.9

Table 4.1: Percentage of double-peaked profiles observed in the population of simulated profiles for different intensity ratios and deviation angles. Weak beaming in assumed ($n = 1$). The deviation angles are in degrees. The random intensity ratios are taken from a uniform distribution of values from 1 to 6.

4.5 Double-Peaked Profiles: Observational Paucity and Parameter Analysis

Only a few of the observed profiles are classified to be double peaked (5 out of 34). Weak x-ray sources suffer of small counting statistics which can lead to false classification of pulse profiles. Sources with a low PF can not be identified to be pulsating and can not be used in the analysis. Tables 4.1 and 4.2 show the fraction of double peaked profiles observed in the simulated populations for different intensity ratios and deviation angles of the secondary pole. For a high intensity ratio ($R = 9$), no double-peaked profiles are observed when weak beaming is considered. The presence of double-peaked profiles increases when strong beaming is considered but drops significantly as the deviation angle is increased. At lower intensity ratios, more double-peaked profiles are observed at all deviation angles when strong beaming is considered. However, the fraction of double-peaked profiles is still much higher than what is observed. Extrapolating from Figure 4.5, the observed sources fall predominantly in the regions corresponding to low intensity ratio for all deviation angles. This paucity of observed double-peaked profiles can be ascribed to the small number of thermally emitting neutron stars from which pulsations have been identified and poor counting statistics of their observed pulse profiles.

To understand the extent of the effect of poor counting statistics on the fraction of observed double-peaked profiles, new profiles that mock the observed ones were created. The simulated profiles are re-binned into 10 bins, normalized, and multiplied with total number of counts to get profiles with high and low number of total counts. The counts in

Deviation	1	3	9	Rand
0	76.3	68.1	38.9	64.2
5	70.7	59.3	17.2	57.6
10	67.6	55.5	8.2	48.4
15	63.6	48.0	5.8	45.9
20	58.7	46.7	3.0	37.2
25	57.5	36.8	3.3	31.0
30	53.8	28.3	2.9	25.9

Table 4.2: Percentage of double-peaked profiles observed in the population of simulated profiles for different intensity ratios and deviation angles. Strong beaming in assumed ($n = 3$). The deviation angles are in degrees. The random intensities ratios are taken from a uniform distribution of values from 1 to 6.

Deviation	1	3	9	Rand
0	73.1	39.5	0.4	30.4
5	66.6	13.2	0.1	23.5
10	59.1	6.7	0.1	20.6
15	55.1	5.2	0.0	13.7
20	48.6	3.6	0.3	12.6
25	46.2	4.2	0.0	9.8
30	42.6	3.5	0.0	8.2

Table 4.3: Percentage of double-peaked profiles observed in the population of simulated, re-binned, and randomized profiles for high counts per bin$(100,000)$, different intensity ratios, and deviation angles. Weak beaming in assumed ($n = 1$). The deviation angles are in degrees. The random intensities ratios are taken from a uniform distribution of values from 1 to 6.

each bin are randomly selected from a Poisson distribution whose mean is the value from the simulated profile. Tables 4.3 and 4.4 show the percentage of profiles classified as double-peaked in the new population generated assuming $100,000$ counts per bin. The number of double peaked profiles is lower than the first simulated population at all deviation angles for all intensity ratios except $R = 9$ for the weak beaming case [1].

Tables 4.5 and 4.6 show the percentage fraction of profiles classified as double-peaked in the new population generated assuming 1000 counts per bin. The number of double-peaked profiles is lower than the original simulated population for low intensity ratios and deviation angles and higher for high intensity ratios and deviation angles. Low counts per bin creates

[1]Only single-peaked profiles were observed for $R = 9$ for weak beaming($n = 1$), thus, adding any randomization will yield double-peaked and complex-structured profiles.

Deviation	1	3	9	Rand
0	68.5	62.1	13.2	56.1
5	67.6	53.2	4.0	47.4
10	65.0	49.9	1.8	40.6
15	60.7	43.1	2.0	39.2
20	56.0	38.4	1.1	29.3
25	55.2	26.9	1.5	25.5
30	51.6	20.9	1.4	21.0

Table 4.4: Percentage of double-peaked profiles observed in the population of simulated, re-binned, and randomized profiles for high counts per bin$(100,000)$, different intensity ratios, and deviation angles. Strong beaming in assumed ($n = 3$). The deviation angles are in degrees. The random intensities ratios are taken from a uniform distribution of values from 1 to 6.

Deviation	1	3	9	Rand
0	70.6	32.1	4.3	31.9
5	72.1	27.4	4.6	31.0
10	64.0	23.3	3.6	28.2
15	61.6	19.9	2.8	23.1
20	58.7	16.7	3.0	21.7
25	54.7	15.2	3.8	20.9
30	51.9	12.8	3.8	17.5

Table 4.5: Percentage of double-peaked profiles observed in the population of simulated, re-binned, and randomized profiles for high counts per bin$(1,000)$, different intensity ratios, and deviation angles. Weak beaming in assumed ($n = 1$). The deviation angles are in degrees. The random intensities ratios are taken from a uniform distribution of values from 1 to 6.

a more pronounced difference in the fraction of profiles classified as double-peaked than the case with higher counts. Thus, data with low counting statistics make it difficult to correctly classify profiles as double-peaked and calculate the corresponding parameters.

The parameters specific to double-peaked profiles: ratio of the two maxima, ratio of the two minima, and the phase difference between the two peaks can be used in combination with other parameters to highlight the asymmetries present profiles and hence the surface thermal map. The ratio of the two maxima is determined by the intensity ratio and the deviation angle of the secondary pole. As the secondary pole is deviated further from the antipodal position, the flux contributions of both poles merge and a lower value of the ratio is obtained. The opposite effect is expected for the ratio of the two minima. The phase difference between

Deviation	1	3	9	Rand
0	70.2	61.2	17.1	54.2
5	70.4	53.7	12.0	48.7
10	70.2	52.0	8.7	46.5
15	68.2	48.7	7.3	44.6
20	63.4	45.7	5.5	38.7
25	60.8	35.9	5.1	32.6
30	57.9	30.2	5.9	27.5

Table 4.6: Percentage of double-peaked profiles observed in the population of simulated, re-binned, and randomized profiles for high counts per bin$(1,000)$, different intensity ratios, and deviation angles. Strong beaming in assumed ($n = 3$). The deviation angles are in degrees. The random intensities ratios are taken from a uniform distribution of values from 1 to 6.

the two peaks is determined solely by the deviation angle of the secondary pole. For the symmetric case, the phase difference is always π irrespective of the intensity ration. Any deviation from the antipodal position results in a lower phase difference depending on the viewing geometry.

Figure 4.8 shows the plots of the phase difference between the peaks of double-peaked profiles versus A2 for different intensity ratios and deviation angles. A high intensity ratio ($r = 9$) results in no or very few double peaked profiles. Smaller values of phase difference are observed at greater deviation angles. Profiles showing a small phase difference have a low value of A2 as the bright regions are concentrated in a smaller area on the stellar surface. For $r = 1$, an almost linear trend is visible between A2 and the phase difference. Profiles showing a higher value of phase difference span a broad range of A2 values but are concentrated towards higher values as it is expected for double peaked profiles. At higher intensity ratios, the flux contribution from one pole dominates over the other one and this results in lower A2 values.

Figure 4.9 shows the ratio of the two maxima (MM-ratio) of double-peaked profiles versus the RMS PF. A higher intensity ratio allows the flux contribution from the primary pole to dominate over the secondary pole and results in a higher MM-ratio. The effect of the deviation angle is characterized by the range of RMS PF spanned at low values of MM-ratio. A larger deviation angle implies a larger RMS PF and a lower MM-ratio. This trend is observed as a larger range of RMS PF is spanned for low MM-ratios as the deviation angle is increased. The relation between the ratio of the two maxima of double-peaked profiles and

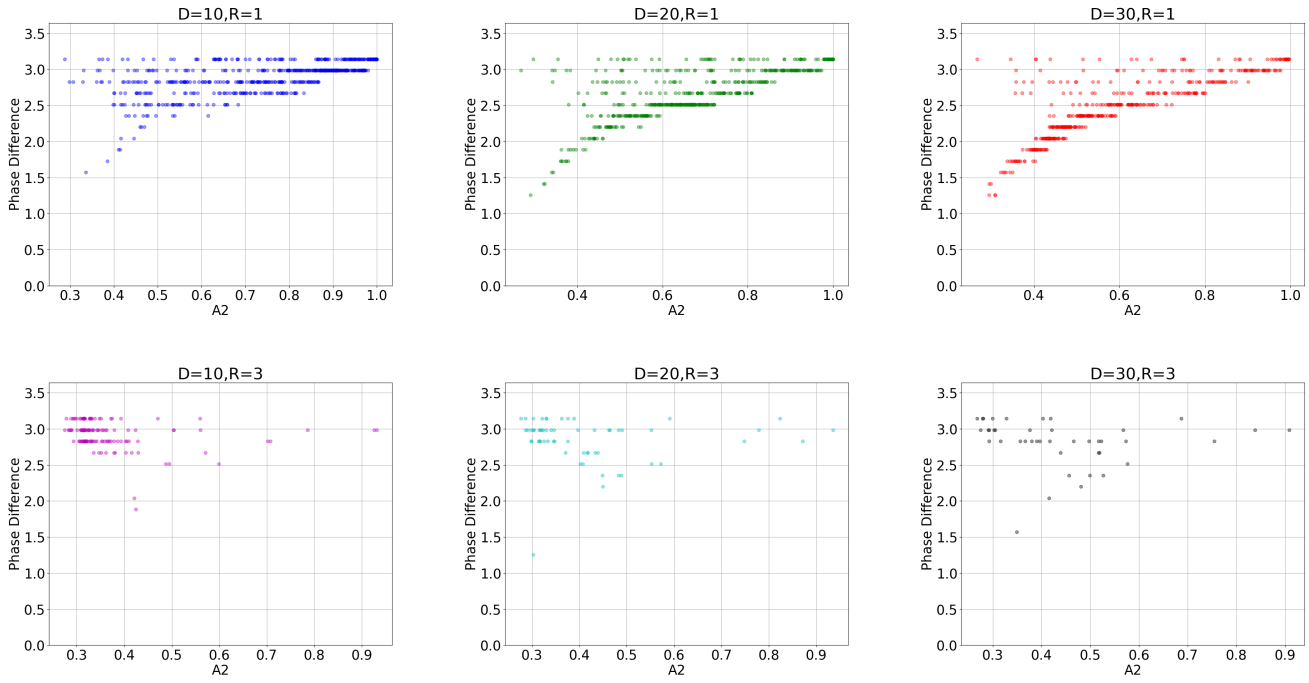

Figure 4.8: The phase difference between peaks of double-peaked profiles versus A2. D is the deviation angle of the secondary pole from the antipodal point and R is the intensity ratio. The phase difference is in radians.

the RMS PF is heavily dependent on the viewing geometry which makes deriving analytical trends difficult.

Such analyses for multiple combinations of parameters specific to double-peaked profiles with other parameters can be performed to study the anisotropies present in the surface thermal map. The observation of very few double-peaked profiles makes it impossible to compare the simulations with the data.

4.6 Effects of Compactness and Beaming Strength

Compactness and beaming strength have direct effects on the shape of the pulse profile and thus on the parameter values. Compactness is described by the GR factor; the more compact a star is, the lower is the GR factor. Beaming strength determines the dependence

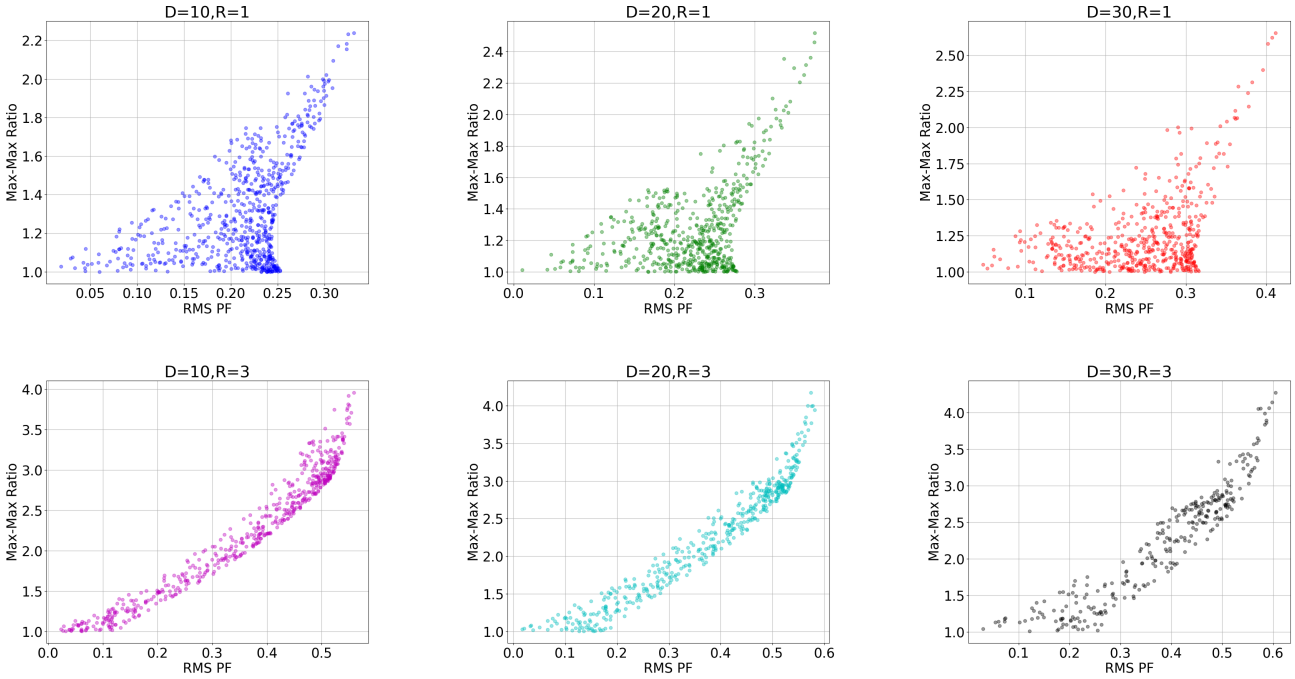

Figure 4.9: The ratio of the two maxima of double-peaked profiles versus RMS PF. D is the deviation angle of the secondary pole from the antipodal point and R is the intensity ratio. The phase difference is in radians.

of intensity of the thermal radiation on the emission angle (θ'). Stronger beaming implies that the radiation from all points on the surface is more directional.
Figures 4.10, 4.11, and 4.12 show the distributions of A2, RMS PF, and skewness of single-peaked profiles respectively. The distributions are made for a population of profiles with an intensity ratio randomly chosen from a uniform distribution from 1 to 9 and a deviation angle randomly chosen from a uniform distribution from 0 to 30 degrees. The lower limit of the GR factor is taken as the limit of light bending approximation described by Beloborodov (2002) [4] which is valid for GR factors$\geq$ 2. GR factor= 8 describes the least compact neutron stars. The strength of beaming is determined by the exponent of the cosine in the beaming function ($\cos^n(\theta')$).

Greater compactness makes a larger area of the stellar surface visible, thus, it reduces the overall flux variation and smoothes the effect of any anisotropies in the surface thermal map on the final shape of the pulse profile. Thus, a lower GR factor results in lower RMS PF, A2, and skewness values. Stronger beaming makes the emission from the surface more

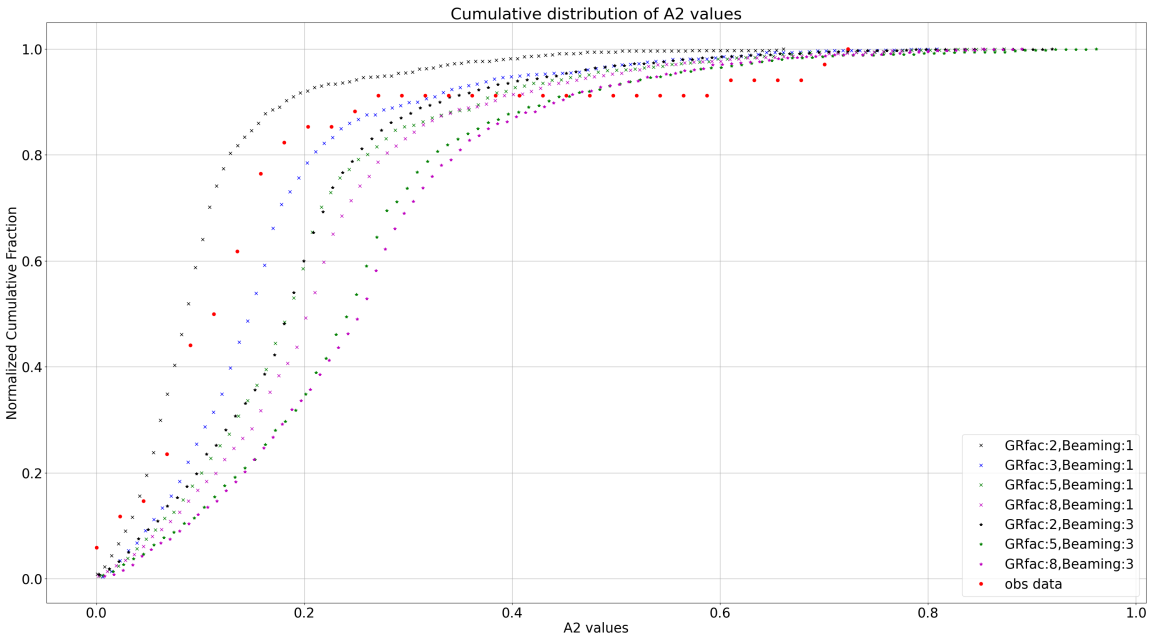

Figure 4.10: Cumulative distributions of A2 for profiles generated for a random intensity ratio selected from a uniform distribution from 1 to 9 and a random deviation angle selected from a uniform distribution between 0 to 30 degrees. GRfac denoted the GR factor (R/r_s) used and beaming denotes the exponent in the beaming function$(\cos^n(\theta'))$. $n = 3$ implies strong beaming and $n = 1$ implies weak beaming. Red points are the observed data.

directional and enhanced the effect of any anisotropy in the surface thermal map on the final pulse profile. This results in larger A2 and RMS PF values. Skewness is dependent on the merging of flux contribution from both poles, depending on the viewing geometry and intensity ratio, the beaming strength can either increase or decrease the skewness of a single-peaked profile. These patterns are evident in the figures 4.10, 4.11, and 4.12. The beaming strength is determined by the properties of the atmosphere present on the neutron star and the GR factor is determined by its mass. A specific selection of these values cannot recreate the distributions of parameters of the observed sample as the atmospheric properties, magnetic field strength, and mass are different for each source.

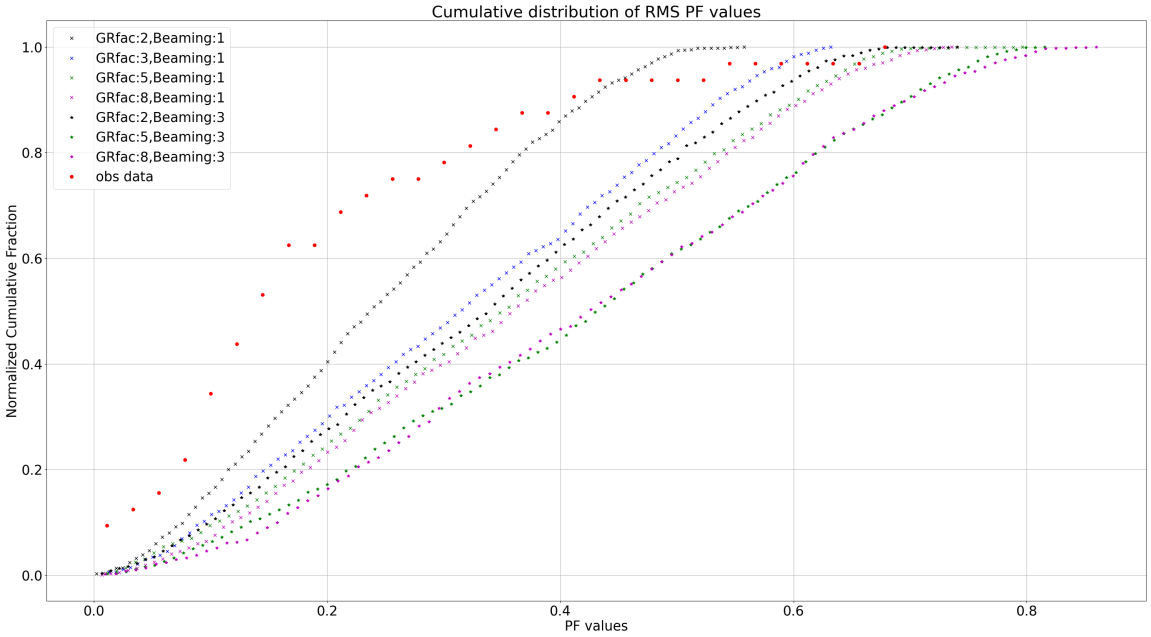

Figure 4.11: Cumulative distributions of RMS PF for profiles generated for a random intensity ratio selected from a uniform distribution from 1 to 9 and a random deviation angle selected from a uniform distribution between 0 to 30 degrees. GRfac denoted the GR factor(R/r_s) used and beaming denotes the exponent in the beaming function($\cos^n(\theta')$). $n = 3$ implies strong beaming and $n = 1$ implies weak beaming. Red points are the observed data.

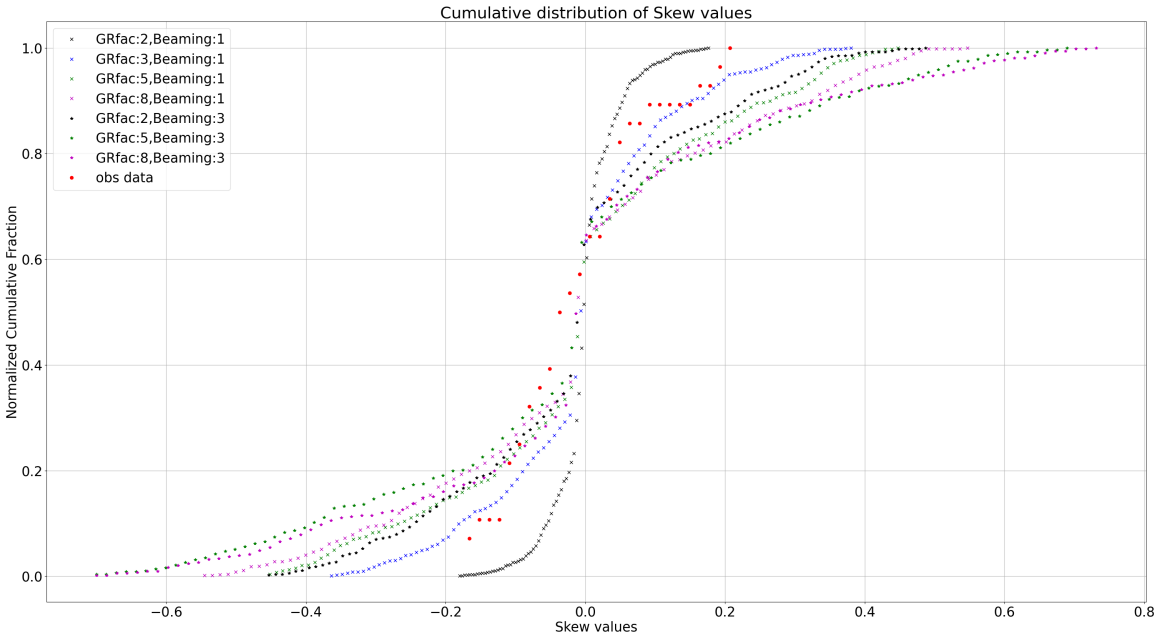

Figure 4.12: Cumulative distributions of skewness values for single-peaked profiles generated for a random intensity ratio selected from a uniform distribution from 1 to 9 and a random deviation angle selected from a uniform distribution between 0 to 30 degrees. GRfac denoted the GR factor(R/r_s) used and beaming denotes the exponent in the beaming function($\cos^n(\theta')$). $n = 3$ implies strong beaming and $n = 1$ implies weak beaming. Red points are the observed data.

Chapter 5

Conclusions

This thesis has been devoted to studying the anisotropic surface thermal distributions of neutron stars. The problem is addressed by considering a thermal map corresponding to the distorted dipolar magnetic field structure (where the second pole is deviated from the antipodal position and its emission is equal to or less bright than that of the primary pole). The distributions of parameters that identify such anisotropies obtained from the simulations are compared with the observed data. The thermal emission from the stellar surface carries a wealth of information as it is affected by the interior composition and mass of the star, the magnetic field structure, and the properties of the atmosphere. The thermal component in the soft x-ray band dominates over the non-thermal component for middle-aged neutron stars. The study of x-ray pulse profiles from these sources can be used to understand the thermal and magnetic structure of neutron stars, derive estimates of their mass and radius, and understand the beaming effects of the atmosphere. The shape of the pulse profiles is principally determined by the surface thermal map and the viewing geometry. Observation of asymmetric pulse profiles (profiles with more than two peaks, double-peaked profiles with unequal peaks, skewed single peak profiles, or double-peaked profiles where the phase separation between the peaks is less than π) indicates the presence of anisotropies in the thermal map that can not be explained by a dipolar magnetic field structure.

An approach that considers a population of pulse profiles generated for randomized viewing geometries with multiple sets of specified initial conditions is required to make a suitable comparison and analysis. Such treatment allows one to appreciate the various factors that affect the final shape of the pulse profiles of thermally emitting neutron stars. Five parame-

ters: the harmonic strength of the second Fourier component (A2), the RMS pulse fraction (RMS PF), skewness of single-peaked profiles, the ratios of the maxima and minima for double-peaked profiles, and phase separation of peaks in double-peaked profiles, are used to quantitatively identify the two anisotropies introduced in the thermal map. The distributions of these parameters for different initial conditions (choice of beaming strength, thermal map, GR factor) exhibit how they yield asymmetric pulse profiles. Immediate comparison with the parameter distributions obtained from the observed data shows significant deviation from the symmetric, dipolar case. The distributions for a population of profiles generated using a random intensity ratio and a random angle of deviation of the second pole from the antipodal point fits the observed data better. This implies that the asymmetric profiles cannot be explained with a single set of parameters (ratio and displacement) equal for all the pulars, but instead a distribution of these values is required.

A pertaining problem in the analysis is the poor statistics of the observed data. First, the sample of thermally emitting neutron stars from which pulsations have been detected is still rather small. Second, many of the pulsars are rather weak X-ray sources, hence the observed pulse profiles suffer of small counting statistics, which can lead to the erroneous classification of the pulse profiles and to poorly determined parameters. Neutron stars with a low PF can not be identified to be pulsating and thus can not be used for this analysis. The limited number of observed sources creates a paucity in the low PF range and reduces the fraction of profiles classified as double-peaked. Thus, the analysis of parameters specific to double-peaked profiles and comparison with data cannot be performed.

The analysis technique used in this thesis describes a general method to study the asymmetries observed in the thermal pulse profiles. This work can be further expanded to incorporate more physical thermal maps derived from models of the magneto-thermal evolution of neutron stars. The thin atmospheres above the stellar surface can be magnetized or non-magnetized and have varying compositions depending on the environment from which the star accretes the material. In a certain range of temperature and field strength, the star's surface can be in a condensed state. Incorporating the effects of complex atmospheres extends the analysis and can explain further asymmetries observed in the pulse profiles. Identification of pulsation from observations of more thermally emitting neutron stars will allow this work to be extended to study double-peaked and complex-structured profiles.
The conclusion of this thesis is that the asymmetric thermal pulse profiles are explained quite well by a distorted-dipole magnetic field topology, which however is not unique for all

the pulsars.

Bibliography

[1] Radiative transfer. By S. Chandrasekhar. London (Oxford University Press) 1950. 8vo. Pp. 393, 35 figures. 35s. *Quarterly Journal of the Royal Meteorological Society*, 76(330):498–498, October 1950.

[2] W. Baade and F. Zwicky. On Super-novae. *Proceedings of the National Academy of Science*, 20(5):254–259, May 1934.

[3] Werner Becker. *X-Ray Emission from Pulsars and Neutron Stars*, pages 91–140. Springer Berlin Heidelberg, Berlin, Heidelberg, 2009.

[4] Andrei M. Beloborodov. Gravitational Bending of Light Near Compact Objects. , 566(2):L85–L88, February 2002.

[5] Slavko Bogdanov, George B. Rybicki, and Jonathan E. Grindlay. Constraints on Neutron Star Properties from X-Ray Observations of Millisecond Pulsars. , 670(1):668–676, November 2007.

[6] S. Burke-Spolaor. Rotating radio transients and their place among pulsars. *Proceedings of the International Astronomical Union*, 8(S291):95–100, 2012.

[7] James Chadwick. The existence of a neutron. *Proceedings of the Royal Society of London. Series A, Containing Papers of a Mathematical and Physical Character*, 136(830):692–708, 1932.

[8] S. Chandrasekhar. The Highly Collapsed Configurations of a Stellar Mass. (Second Paper.). *Monthly Notices of the Royal Astronomical Society*, 95(3):207–225, 01 1935.

[9] H.-Y. Chiu and E. E. Salpeter. Surface x-ray emission from neutron stars. *Phys. Rev. Lett.*, 12:413–415, 1964.

[10] J. Daligault and S. Gupta. Electron–ion scattering in dense multi-component plasmas: Application to the outer crust of an accreting neutron star. *The Astrophysical Journal*, 703(1):994, sep 2009.

[11] Rafael C. R. de Lima, Jaziel G. Coelho, Jonas P. Pereira, Claudia V. Rodrigues, and Jorge A. Rueda. Evidence for a multipolar magnetic field in SGR j1745-2900 from x-ray light-curve analysis. *The Astrophysical Journal*, 889(2):165, February 2020.

[12] Psaltis DeDeo and Narayan. General Relativistic Constraints on Emission Models of Anomalous X-Ray Pulsars. , 599(2):346–352, October 2001.

[13] Geppert, U., Küker, M., and Page, D. Temperature distribution in magnetized neutron star crusts. *A&A*, 426(1):267–277, 2004.

[14] Riccardo Giacconi, Herbert Gursky, Frank R. Paolini, and Bruno B. Rossi. Evidence for x rays from sources outside the solar system. *Phys. Rev. Lett.*, 9:439–443, Dec 1962.

[15] Thomas Gold. Rotating Neutron Stars and the Nature of Pulsars. , 221(5175):25–27, January 1969.

[16] A. HEWISH, S. J. BELL, J. D. H. PILKINGTON, P. F. SCOTT, and R. A. COLLINS. Observation of a rapidly pulsating radio source. *Nature*, 217(5130):709–713, February 1968.

[17] Jeremy S. Heyl and Lars Hernquist. Almost analytic models of ultramagnetized neutron star envelopes. , 300(2):599–615, October 1998.

[18] Chin-Ping Hu, C-Y Ng, and Wynn C G Ho. A systematic study of soft X-ray pulse profiles of magnetars in quiescence. *Monthly Notices of the Royal Astronomical Society*, 485(3):4274–4286, 03 2019.

[19] R. N. Manchester. Millisecond pulsars, their evolution and applications. *Journal of Astrophysics and Astronomy*, 38(3), September 2017.

[20] Sandro Mereghetti, José A. Pons, and Andrew Melatos. Magnetars: Properties, Origin and Evolution. , 191(1-4):315–338, October 2015.

[21] J. R. Oppenheimer and G. M. Volkoff. On massive neutron cores. *Phys. Rev.*, 55:374–381, Feb 1939.

[22] F. Pacini. Neutron Stars, Pulsars and Supernova Remnants: concluding remarks. In W. Becker, H. Lesch, and J. Trümper, editors, *Neutron Stars, Pulsars, and Supernova Remnants*, page 300, January 2002.

[23] Dany Page. Surface Temperature of a Magnetized Neutron Star and Interpretation of the ROSAT Data. I. Dipolar Fields. , 442:273, March 1995.

[24] Alexander Y. Potekhin, José A. Pons, and Dany Page. Neutron Stars—Cooling and Transport. , 191(1-4):239–291, October 2015.

[25] Potekhin, A. Y. and Chabrier, G. Magnetic neutron star cooling and microphysics. *A&A*, 609:A74, 2018.

[26] Nanda Rea, José A. Pons, Diego F. Torres, and Roberto Turolla. The Fundamental Plane for Radio Magnetars. , 748(1):L12, March 2012.

[27] L. Strüder, U. Briel, K. Dennerl, R. Hartmann, E. Kendziorra, N. Meidinger, E. Pfeffermann, C. Reppin, B. Aschenbach, W. Bornemann, H. Bräuninger, W. Burkert, M. Elender, M. Freyberg, F. Haberl, G. Hartner, F. Heuschmann, H. Hippmann, E. Kastelic, S. Kemmer, G. Kettenring, W. Kink, N. Krause, S. Müller, A. Oppitz, W. Pietsch, M. Popp, P. Predehl, A. Read, K. H. Stephan, D. Stötter, J. Trümper, P. Holl, J. Kemmer, H. Soltau, R. Stötter, U. Weber, U. Weichert, C. von Zanthier, D. Carathanassis, G. Lutz, R. H. Richter, P. Solc, H. Böttcher, M. Kuster, R. Staubert, A. Abbey, A. Holland, M. Turner, M. Balasini, G. F. Bignami, N. La Palombara, G. Villa, W. Buttler, F. Gianini, R. Lainé, D. Lumb, and P. Dhez. The European Photon Imaging Camera on XMM-Newton: The pn-CCD camera. , 365:L18–L26, January 2001.

[28] K. S. Thorne and A. N. Zytkow. Stars with degenerate neutron cores. I. Structure of equilibrium models. , 212:832–858, March 1977.

[29] Richard C. Tolman. Static solutions of einstein's field equations for spheres of fluid. *Phys. Rev.*, 55:364–373, Feb 1939.

[30] M. J. L. Turner, A. Abbey, M. Arnaud, M. Balasini, M. Barbera, E. Belsole, P. J. Bennie, J. P. Bernard, G. F. Bignami, M. Boer, U. Briel, I. Butler, C. Cara, C. Chabaud, R. Cole, A. Collura, M. Conte, A. Cros, M. Denby, P. Dhez, G. Di Coco, J. Dowson, P. Ferrando, S. Ghizzardi, F. Gianotti, C. V. Goodall, L. Gretton, R. G. Griffiths, O. Hainaut, J. F. Hochedez, A. D. Holland, E. Jourdain, E. Kendziorra, A. Lagostina,

R. Laine, N. La Palombara, M. Lortholary, D. Lumb, P. Marty, S. Molendi, C. Pigot, E. Poindron, K. A. Pounds, J. N. Reeves, C. Reppin, R. Rothenflug, P. Salvetat, J. L. Sauvageot, D. Schmitt, S. Sembay, A. D. T. Short, J. Spragg, J. Stephen, L. Strüder, A. Tiengo, M. Trifoglio, J. Trümper, S. Vercellone, L. Vigroux, G. Villa, M. J. Ward, S. Whitehead, and E. Zonca. The European Photon Imaging Camera on XMM-Newton: The MOS cameras. , 365:L27–L35, January 2001.

[31] D. Viganò, N. Rea, J. A. Pons, R. Perna, D. N. Aguilera, and J. A. Miralles. Unifying the observational diversity of isolated neutron stars via magneto-thermal evolution models. , 434(1):123–141, September 2013.

[32] D. Viganò and J. A. Pons. Central compact objects and the hidden magnetic field scenario. *Monthly Notices of the Royal Astronomical Society*, 425(4):2487–2492, 10 2012.

[33] Silvia Zane and Roberto Turolla. Unveiling the thermal and magnetic map of neutron star surfaces though their X-ray emission: method and light-curve analysis. *Monthly Notices of the Royal Astronomical Society*, 366(3):727–738, 03 2006.

[34] Pavlov Zavlin and Trumper. X-Ray Emission from the Radio-quiet Neutron Star in Puppis A. , 525(2):959–967, November 1999.